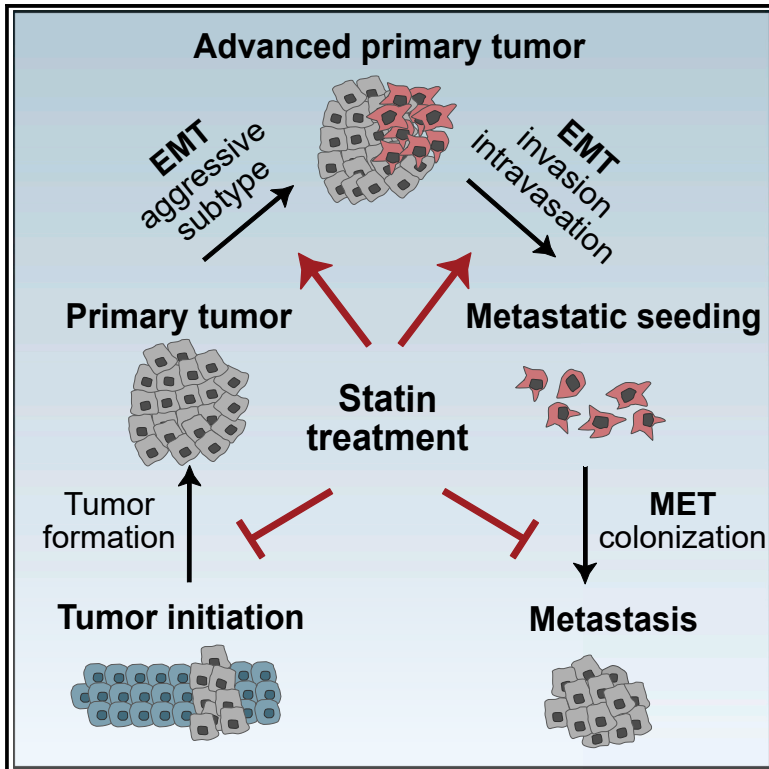


## Statins affect cancer cell plasticity with distinct consequences for tumor progression and metastasis

### Graphical abstract



### Authors

Madeleine Dorsch, Manuela Kowalczyk, Mélanie Planque, ..., Sarah-Maria Fendt, Perihan Nalbant, Barbara M. Grüner

### Correspondence

barbara.gruener@uk-essen.de

### In brief

Dorsch et al. identify statins as potent modulators of cancer cell plasticity and demonstrate that cholesterol pathway inhibition induces a mesenchymal cell shift in cancer cells. They show that statin-induced EMT promotes metastatic seeding on one hand but unexpectedly counteracts tumor and metastasis formation on the other hand.

### Highlights

- Statins induce a partial EMT phenotype in PDAC, lung cancer, and colon cancer
- Partial EMT and reduced cellular plasticity can drive apoptosis or block MET
- Cancer cells overcome statin-induced apoptosis by activating ERK
- Statins increase metastatic seeding but reduce tumor formation and metastatic growth



## Article

# Statins affect cancer cell plasticity with distinct consequences for tumor progression and metastasis

Madeleine Dorsch,<sup>1</sup> Manuela Kowalczyk,<sup>2</sup> Mélanie Planque,<sup>3,4</sup> Geronimo Heilmann,<sup>5</sup> Sebastian Urban,<sup>1</sup> Philip Dujardin,<sup>1</sup> Jan Forster,<sup>6,7</sup> Kristina Ueffing,<sup>1</sup> Silke Nothdurft,<sup>1</sup> Sebastian Oeck,<sup>1</sup> Annika Paul,<sup>1</sup> Sven T. Liffers,<sup>8</sup> Farnusch Kaschani,<sup>5</sup> Markus Kaiser,<sup>5</sup> Alexander Schramm,<sup>1</sup> Jens T. Siveke,<sup>8,9</sup> Monte M. Winslow,<sup>10,11</sup> Sarah-Maria Fendt,<sup>3,4</sup> Perihan Nalbant,<sup>2</sup> and Barbara M. Grüner<sup>1,7,12,\*</sup>

<sup>1</sup>Department of Medical Oncology, West German Cancer Center, University Hospital Essen at the University Duisburg-Essen, Duisburg, Germany

<sup>2</sup>Department of Molecular Cell Biology, Center for Medical Biotechnology, University of Duisburg-Essen, Duisburg, Germany

<sup>3</sup>Laboratory of Cellular Metabolism and Metabolic Regulation, VIB-KU Leuven Center for Cancer Biology, VIB, Leuven, Belgium

<sup>4</sup>Laboratory of Cellular Metabolism and Metabolic Regulation, Department of Oncology, KU Leuven and Leuven Cancer Institute (LKI), Leuven, Belgium

<sup>5</sup>Department of Chemical Biology, Center for Medical Biotechnology, University of Duisburg-Essen, Duisburg, Germany

<sup>6</sup>Department of Genome Informatics, Institute for Human Genetics, University of Duisburg-Essen, Duisburg, Germany

<sup>7</sup>German Cancer Consortium (DKTK) partner site Essen, Essen, Germany

<sup>8</sup>Bridge Institute of Experimental Tumor Therapy, West German Cancer Center, University Medicine Essen, Essen, Germany

<sup>9</sup>Division of Solid Tumor Translational Oncology, German Cancer Research Center (DKFZ) and German Cancer Consortium (DKTK), partner site Essen, Heidelberg, Germany

<sup>10</sup>Department of Genetics, Stanford University School of Medicine, Stanford, CA, USA

<sup>11</sup>Department of Pathology, Stanford University School of Medicine, Stanford, CA, USA

<sup>12</sup>Lead contact

\*Correspondence: [barbara.gruener@uk-essen.de](mailto:barbara.gruener@uk-essen.de)

<https://doi.org/10.1016/j.celrep.2021.110056>

## SUMMARY

Statins are among the most commonly prescribed drugs, and around every fourth person above the age of 40 is on statin medication. Therefore, it is of utmost clinical importance to understand the effect of statins on cancer cell plasticity and its consequences to not only patients with cancer but also patients who are on statins. Here, we find that statins induce a partial epithelial-to-mesenchymal transition (EMT) phenotype in cancer cells of solid tumors. Using a comprehensive STRING network analysis of transcriptome, proteome, and phosphoproteome data combined with multiple mechanistic *in vitro* and functional *in vivo* analyses, we demonstrate that statins reduce cellular plasticity by enforcing a mesenchymal-like cell state that increases metastatic seeding ability on one side but reduces the formation of (secondary) tumors on the other due to heterogeneous treatment responses. Taken together, we provide a thorough mechanistic overview of the consequences of statin use for each step of cancer development, progression, and metastasis.

## INTRODUCTION

Molecular and phenotypic changes in tumor cells are collectively referred to as cellular plasticity. Cellular plasticity is a common requirement for cancer cells to progress, adapt into different subtypes, respond to treatment, and gain metastatic ability. Epithelial-to-mesenchymal transition (EMT) is one of the best-described programs of cellular plasticity and considered a crucial step to enhance tumor progression and to initiate the metastatic process (Yuan et al., 2019). Post-initiation, metastatic cells require a dynamic and critical reversal in cellular phenotype (mesenchymal-to-epithelial transition [MET]), enabling the colonization of distant organs. These dynamic processes are termed epithelial-mesenchymal plasticity (EMP), an ability that is essential for metastases but that also affects cancer initiation, progres-

sion, and therapy responses (Gupta et al., 2019). EMP is not a single-cell state with binary readout, defined by either epithelial or mesenchymal cell markers (Williams et al., 2019; Karacosta et al., 2019), but rather comprises a combination of cell states that display partial EMT phenotypes with both epithelial and mesenchymal characteristics (Gupta et al., 2019; Karacosta et al., 2019; Williams et al., 2019). This plastic cellular state of cancer cells contributes to the challenge of not only identifying effective therapies and fully comprehending the underlying mechanisms of cancer progression and metastasis but also understanding the full impact of (targeted) anti-cancer therapies and other medications on cancer patients.

Metastasis is a complex multistep process that requires high cellular plasticity (Steeg, 2006; Massagué and Obenauf, 2016; Fares et al., 2020). It is highly likely that commonly



used medications might impact the behavior of (metastatic) cancer cells due to the cancer cells' high non-genetic cellular plasticity (Yuan et al., 2019). To identify drugs that could impact cellular plasticity, we adapted a previously established multiplexed small-molecule screening platform to enable high-throughput, unbiased, and quantitative identification of regulators of metastatic seeding of cancer cells *in vivo* (Grüner et al., 2016). From a library of 624 Food and Drug Administration (FDA)-approved inhibitors, we identified statins as a drug class that significantly inhibits the metastatic ability of pancreatic cancer (pancreatic ductal adenocarcinoma [PDAC]) cells *in vitro* and *in vivo*. We find that although statin treatment initially enhances the ability of cancer cells to migrate and resist anoikis resulting in increased metastatic seeding, these cells are then unable to revert to a more epithelial-like cell state that leads to decreased secondary tumor or metastasis formation. Thus, the enforced induction of EMT by statins has distinct effects on cancer cells at different stages of tumor initiation, progression, and metastasis, a finding that clinicians need to consider when prescribing statins to their (cancer) patients.

## RESULTS

### Multiplexed *in vivo* screening identifies statins as potential regulators of metastasis

To analyze the impact of drugs already in clinical use on cancer cell plasticity, we used an *in vivo* multiplexed small-molecule screening platform to quantify the impact of FDA-approved drugs on metastatic seeding (Grüner et al., 2016). In this approach, uniquely barcoded variants of a murine metastatic pancreatic cancer cell line are treated individually with drugs for ~40 h followed by pooling and intravenous transplantation into syngeneic recipient mice (Figure S1A; Grüner et al., 2016). Barcode sequencing of the pre-injection pool and cancer cells in the lungs 2 days after injection can uncover drugs that impact metastatic seeding ability. In total, we screened 624 compounds and uncovered 39 hits (6.25% hit rate) that significantly lowered the incidence of metastatic seeding in the lungs of syngeneic recipient mice (Figure 1A; Table S1). To differentiate specific effects on metastatic seeding from general toxicity, we performed *in vitro* viability assays and calculated the relative "metastatic selectivity" for each compound defined as the ratio of reduced metastatic ability *in vivo* to the overall loss of viability *in vitro* (Figure 1B; Table S1; STAR Methods; Grüner et al., 2016). Based on metastatic selectivity, compound class diversity, and compounds with known molecular targets, we chose 14 top candidates for a secondary dose-response validation screen (Figures S1B and S1C). Fluvastatin emerged as one of the top validated hits, demonstrating an inhibition of metastatic seeding ability in a dose-dependent manner *in vivo* without general toxicity (Figures 1C and S1D).

Our screening method identifies drugs that impact the earlier stages of metastasis, including survival in circulation as well as adhesion and extravasation at a secondary site (Grüner et al., 2016). To validate the effects of fluvastatin in a model that recapitulates the entire metastatic cascade, mice with established tumors from human ASPC1 cells were treated with fluvastatin

or vehicle once the volume of primary tumors exceeded 100 mm<sup>3</sup>, which is at the onset of metastases in this model (Figure 1D; Grüner et al., 2016). Subcutaneous tumor growth was not significantly different between the fluvastatin-treated and control mice. Even though previous studies suggested otherwise (Gbelcová et al., 2008), proliferation in primary subcutaneous tumors was similar in treated and control animals (Figures 1E, S1E, and S1F). Fluvastatin treatment reduced metastases to the lungs >2-fold, as shown by fluorescence microscopy, GFP immunohistochemistry, and flow cytometry analysis of dissociated lung lobes (Figures 1F–1H). Thus, fluvastatin reduced pancreatic cancer metastases *in vivo* without influencing primary tumor growth.

### Statin treatment induces a mesenchymal cell morphology in pancreas, lung, and colon cancer cells

To uncover the impact of statins on cells growing *in vitro* in 2D and 3D, three human PDAC cell lines with different morphologies were subjected to fluvastatin treatment. Fluvastatin induced cellular morphology changes reminiscent of EMT, albeit with partially distinct effects across cell lines (Figures 2A, S2A, and S2B). In addition, fluvastatin treatment of PDAC cells grown in 3D resulted in the loss of sphere-forming ability and loosened cell contacts, accompanied by a substantial increase in sphere area due to increased distance between individual cells (Figures 2B and 2C).

Statins inhibit the rate limiting step of the intracellular cholesterol synthesis by blocking the 3-hydroxy-3-methylglutaryl coenzyme A (CoA) reductase (HMGCR) and thus the conversion of HMG-CoA to mevalonic acid (MVA) (Brown and Goldstein, 1980). Importantly, the phenotypic changes observed in 2D and 3D were reverted upon addition of MVA (Figures 2A–2C, S2A, and S2B), confirming that HMGCR is the target of statins in metastatic PDAC. In addition, lovastatin and cerivastatin treatment recapitulate these effects, which is consistent with a common mode of action for statins (Figures 2D, 2E, and S2C–S2H). Interestingly, statin treatment led to comparable effects on lung cancer and colon cancer cells both in 2D and 3D culture (Figures 2F, 2G, and S2I–S2L). Inhibition of sphere formation and phenotypic changes were strictly dependent on the presence of fluvastatin, as spheres started to rebuild within 7 days upon depletion of fluvastatin (Figure 2H). Similarly, phenotypic changes were reversible upon addition of MVA (Figure 2I, middle and bottom panel; Figure S2M). Of note, addition of fluvastatin to pre-existing spheres had no effect on 3D sphere architecture (Figure 2I, top panel). Importantly, fluvastatin treatment did not affect cell growth, indicating that the phenotypic effects were not due to differences in cell viability or proliferation (Figures S2N–S2P).

### Cholesterol pathway inhibition induces profound changes in signaling networks

To uncover the underlying molecular mechanisms that drive the dramatic statin-mediated switch in cell morphology, we performed independent microarray, total proteome, and phosphoproteome analyses of ASPC1 cells treated with fluvastatin or vehicle. Genes and proteins that were upregulated 1.5-fold between treatment and control groups were subjected to STRING (search tool for recurring instances of neighbouring genes)

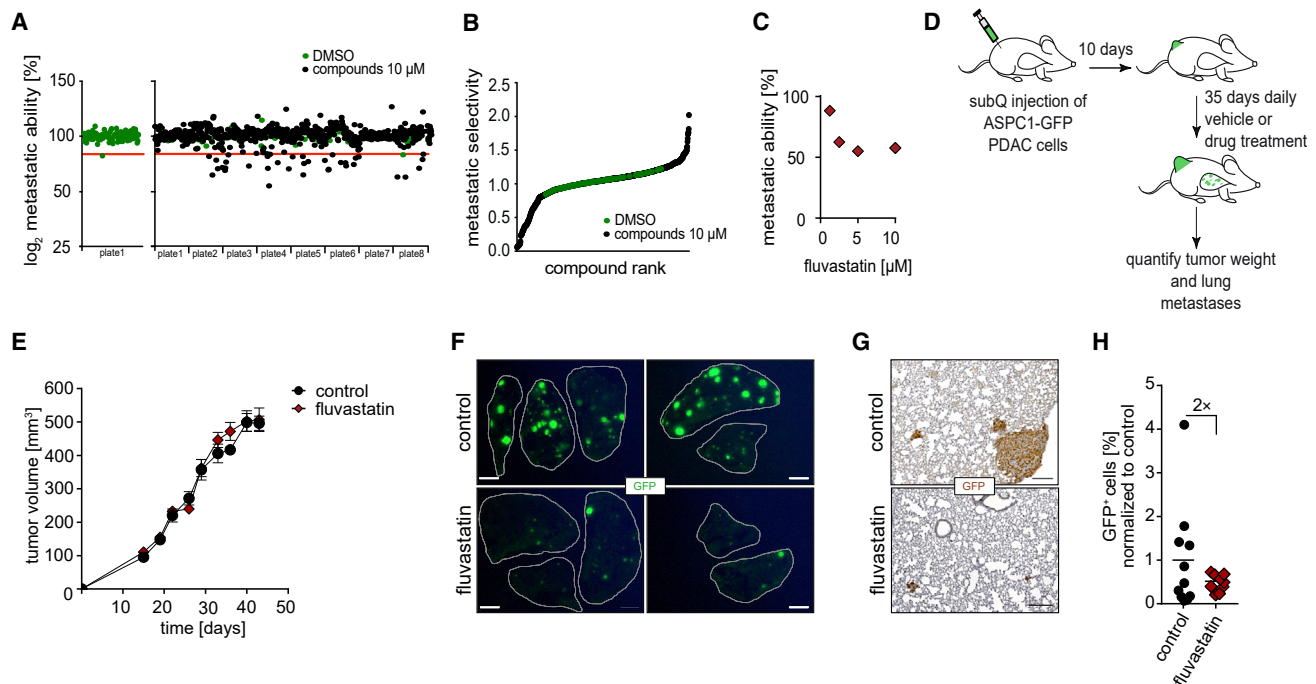


**Figure 1. Multiplexed *in vivo* screening reveals fluvastatin as an inhibitor of PDAC metastasis *in vivo***

(A) Screening of 624 FDA-approved drugs distributed across 8 96-well plates. Each black dot represents one compound. The red line indicates a 20% loss of metastatic ability.

(B) Metastatic selectivity of the FDA-approved drugs within the initial screen.

(C) Dose-dependent effect of fluvastatin on metastatic ability of 0688M cells after 72 h of pretreatment.

(D) Schematic of the *in vivo* metastasis model.

(E) Tumor volume of subcutaneous tumors in mice treated as depicted in (D); n = 7 mice per group, symbols indicate the mean, error bars indicate  $\pm$  SEM.

(F) Representative fluorescent image of the five lung lobes of mice treated as depicted in (D); scale bars: 1,000  $\mu$ m.

(G) Representative images of immunohistochemistry for GFP in the lungs of recipient mice; scale bars: 100  $\mu$ m.

(H) Quantification of GFP<sup>+</sup> cancer cells in metastases by flow cytometry (fluorescence-activated cell sorting [FACS]); data are from two independent experiments normalized to control group; each dot represents a mouse, the black line is the mean; n = 10–11 mice per group.

See also Figure S1 and Table S1.

analysis for network visualization. To expand the STRING networks and improve significant clustering, we added the significantly ( $p < 0.05$ ) upregulated phosphorylated proteins after both 48 h and 15 min of fluvastatin treatment. A strict confidence interval of 0.9 was set to display only strong protein interactions. Overall, results of microarray, proteome, and phosphorylated proteome analyses were highly consistent, with many proteins being significantly upregulated in at least two independent datasets (Figure 3A).

One of the main functional protein clusters that were upregulated by fluvastatin treatment included members of the cholesterol metabolism protein family (Figure 3A). Gene Set Enrichment Analysis (GSEA) of the microarray data confirmed an upregulation of the cholesterol homeostasis signaling pathway in statin-treated cells (Figure 3B; Table S2). Additionally, qPCR analysis of cancer cells treated with fluvastatin or cerivastatin confirmed that statins increase the expression of *HMGCR*, consistent with published observations (Gbelcová et al., 2017b). *HMGCR* induction could be reverted upon addition of MVA (Figures 3C, S3A, and S3B). Furthermore, Acyl-CoA Synthetase Short Chain Family Member 2 (*ACSS2*) that catalyzes the activation of acetate for use in lipid synthesis and energy generation (Schug et al., 2015)

was highly upregulated at both the mRNA and protein level and was phosphorylated upon statin treatment (Figure 3A). We hypothesized that *HMGCR* and *ACSS2* upregulation might counteract statin-mediated inhibition of intracellular *de novo* cholesterol synthesis, which was also supported by data in a breast cancer trial that discovered an upregulation of *HMGCR* upon statin treatment (Bjarnadottir et al., 2013).

To analyze the cholesterol levels in pancreatic cancer cells, we performed mass spectrometry (MS) analysis of ASPC1 cells treated with fluvastatin or vehicle. Interestingly, total cholesterol levels were unchanged in statin-treated cancer cells (Figure 3D). However, <sup>13</sup>C-labeling of cells treated with fluvastatin, MVA, fluvastatin plus MVA, or control demonstrated that fluvastatin indeed inhibited *de novo* cholesterol synthesis. As expected, supplementing MVA reduced <sup>13</sup>C-glucose incorporation into cholesterol, as it provided a second unlabeled carbon source. Simultaneous addition of MVA and fluvastatin also inhibited *de novo* cholesterol synthesis, demonstrating that the concentration of fluvastatin was still able to inhibit *HMGCR*, despite increased expression levels (Figure 3E). Thus, the statin-mediated phenotypic changes in cancer cells are not due to inhibition of *HMGCR* itself or low cellular cholesterol levels but rather due

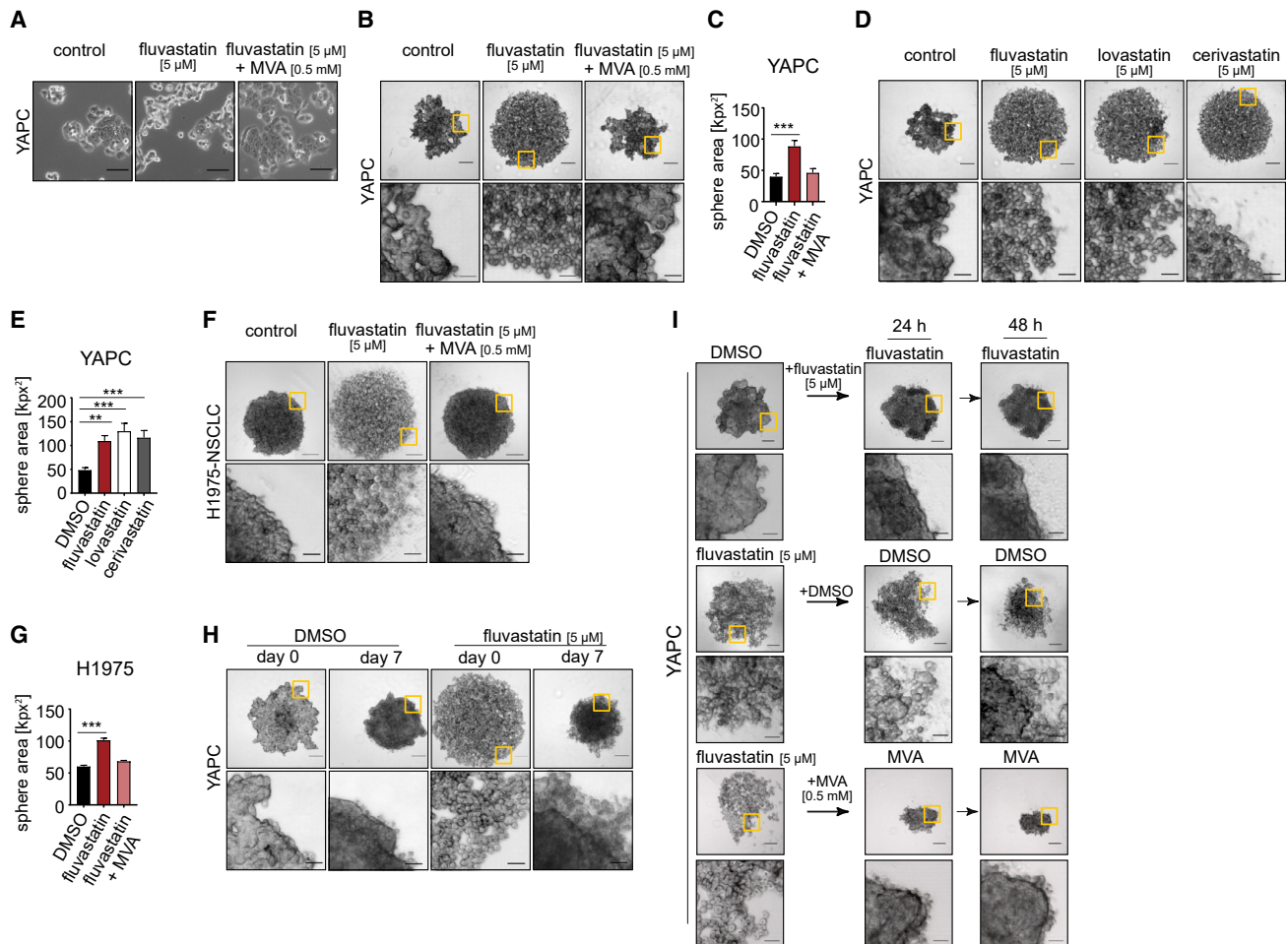


**Figure 2. Cholesterol pathway inhibition induces a shift in cellular morphology**

(A) YAPC cells in two-dimensional (2D) cell culture after 48 h of treatment as indicated.

(B–E) Sphere formation (B and D) and sphere area quantification (C and E) of YAPC cells with 48 h pretreatment as indicated.

(F and G) Sphere formation (F) and sphere area quantification (G) of H1975 cells with 48 h pretreatment as indicated.

(H) Sphere formation for 7 days of YAPC cells with 48 h pretreatment as indicated.

(I) Sphere formation of YAPC cells with 48 h pretreatment as indicated; then the medium was changed and indicated drugs were added for the indicated times.

Scale bars: 75 μm (top panel), 20 μm (bottom panel); yellow boxes: area chosen for magnification below; one representative out of three independent experiments is depicted; bar graphs indicate the mean; error bars indicate ± SEM. Significance test: one-way ANOVA. See also Figure S2.

to the general MVA depletion downstream of HMGCR in the cancer cells and therefore inhibition of *de novo* cholesterol biosynthesis. It is possible that the distribution of membrane cellular cholesterol could be altered upon statin treatment, thereby influencing cellular signaling (Zhang et al., 2019a; Luu et al., 2013). This idea is corroborated by the fact that statin treatment also upregulated the expression of the low-density lipoprotein (LDL) receptor, as well as of many proteins involved in vesicular transport, which allows cells to increase the transport of extracellular cholesterol into the cells (Figure 3A; Greenwood et al., 2006).

### ERK activation counteracts statin-induced apoptosis

In addition to cholesterol biosynthesis, GSEA of fluvastatin-treated cells identified a significant upregulation of genes involved in apoptosis, as described previously (Hoque et al., 2008; Alizadeh et al., 2017; Wong et al., 2001; Figure 3F). Func-

tional analyses revealed cell-line-specific anti-apoptotic responses upon fluvastatin treatment (Figures 3G–3I and S3C–S3H), rendering it unlikely that decreased metastasis formation *in vivo* could be solely attributed to apoptotic programs induced by fluvastatin. Instead, as also suggested by STRING and GSEA analyses and confirmed by western blotting, genes involved in KRAS signaling and ERK activation were increased upon fluvastatin treatment in ASPC1 and Panc89 cells (Figures 3J and 3K). Interestingly, a lack of ERK activation corresponded with high levels of apoptosis induction in YAPC cells. Correspondingly, a combination treatment with both the MEK inhibitor trametinib and statin further increased the apoptosis-inducing effect of trametinib treatment alone in ASPC1 cells (Figures 3L and 3M). In YAPC cells, where ERK was not activated upon statin treatment, trametinib treatment had no additional effect on apoptosis levels compared to statin treatment alone (Figures 3N and 3O). Thus,

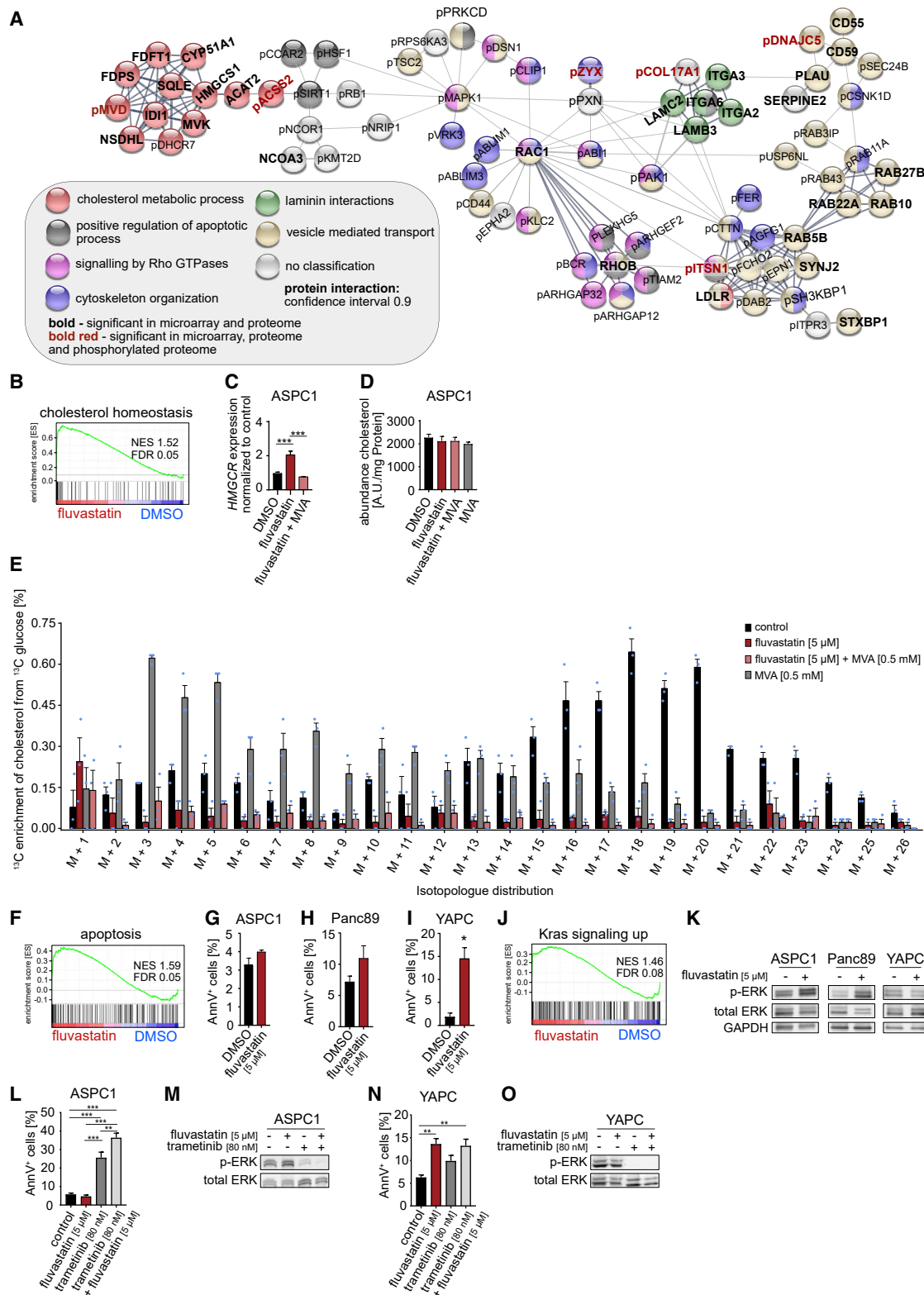


**Figure 3. Statin treatment inhibits *de novo* cholesterol synthesis and affects essential signaling pathways and cellular programs**

(A) STRING analysis of ASPC1 cells treated with 5 μM fluvastatin or control for 48 h. Cells were subjected to microarray analysis, total proteome analysis, and phosphoproteome analysis after 48 h of treatment as well as phosphoproteome analysis after 15 min of treatment each in independently performed experiments.

(legend continued on next page)

activation of ERK signaling could also counteract the induction of apoptosis upon statin treatment and seems to be cell line dependent.

### Cholesterol pathway inhibition induces an EMT-like cell state

Changes in cellular morphology are typically accompanied by cytoskeletal alterations (Wickstead and Gull, 2011). Indeed, the STRING analysis identified multiple components of the cytoskeleton and Rho protein signaling that were upregulated upon cholesterol pathway inhibition (Figure 3A). Also, the scaffolding protein Intersectin 1 (ITSN1) was upregulated at both the mRNA and protein level and was phosphorylated upon statin treatment (Figure 3A). ITSN1 is known to regulate vesicular transport (O'Bryan, 2010). In addition, ITSN1 is a guanine nucleotide exchange factor (GEF) for the Rho GTPase family protein Cdc42 and is therefore directly involved in signaling pathways that control the actin cytoskeleton (O'Bryan, 2010). The STRING analysis pointed to ITSN1 as a major transmitter of the signaling between cholesterol homeostasis and cytoskeletal morphology affected by statin treatment (Figure 3A). GSEA analysis revealed an upregulation of genes involved in actin cytoskeleton reorganization (Figure 4A). In agreement with this, F-Actin staining of ASPC1, YAPC, and Panc89 cells revealed marked cytoskeletal rearrangements upon statin treatment. In particular, a substantial subset of statin-treated ASPC1 cells formed flat actin protrusions and lost their peripheral actin ring (Figures 4B and S4A). Furthermore, statin treatment of Panc89 cells led to a loss of actin filaments, and they were reminiscent of contractile stress fibers. YAPC cells generated pronounced peripheral actin bundles upon statin exposure, adopting the mesenchymal phenotype of untreated ASPC1 cells (Figure S4A).

GSEA analysis suggested a statin-induced upregulation of EMT genes (Figure 4C), exemplified by the MVA-reversible induction of the mesenchymal transcription factor SLUG, as confirmed by qPCR (Figures 4D and S4B). Surprisingly, fluvastatin and cerivastatin induced the expression of E-cadherin at the mRNA and protein level, which again could be reverted upon addition of MVA (Figures 4E, S4C, and S4D). E-cadherin expression increased 48 to 96 h after treatment with fluvastatin (Figures 4F and S4E). Also, E-cadherin upregulation required continuous exposure to drug (Figure S4F). Interestingly, immunostaining for

E-cadherin in statin-treated cells did not indicate a change in the membrane localization of E-cadherin per se, albeit the number of cells with functional cell-cell contacts was significantly reduced (Figures 4G and S4G). These data indicate that although E-cadherin expression is upregulated upon statin treatment, it does not result in a more epithelial-like phenotype with increased cellular contacts but rather has the opposite effect.

Recent studies have suggested a more dynamic definition of epithelial and mesenchymal cell states and a corresponding expression of markers (Williams et al., 2019; Padmanaban et al., 2019; Gupta et al., 2019; Karacosta et al., 2019). We investigated whether our datasets could be used to identify the statin-induced cell state within this context. We compared the relative expression of EMT markers within our microarray data and generated relative expression curves representing the defined EMT states. Indeed, when comparing the expression of the 6 analyzed EMT markers (CDH1, Vimentin, CD44, MUC1, TWIST1, and CD24) between ASPC1 cells treated with fluvastatin and control, we confirmed an increased expression of the mesenchymal markers Vimentin, CD44, and TWIST1 but also of the epithelial marker CDH1 in fluvastatin-treated cells (Figure S4H). Indeed, statin-treated ASPC1 cells are in a state most comparable to a partial EMT state (Figures 4H and S4I). Furthermore, even though E-cadherin expression is upregulated in statin-treated cells, its relative expression in comparison to the other EMT markers fits these trajectories very well, further indicating that the increase in E-cadherin expression is not controversial to the observed EMT-like cell shift. It has previously been shown that the loss of E-cadherin expression as a marker of metastatic cells is an oversimplification, and many metastases still contain high levels of E-cadherin. Also, epithelial cells expressing E-cadherin can become invasive and metastasize without undergoing a full EMT in cancers (Bukholm et al., 2000; Hollestelle et al., 2013). It is unknown to which extent the statin-mediated upregulation of E-cadherin observed in our study serves to further promote or counteract the functional EMT-like switch in cell state.

### Statins have a dual effect on metastatic ability and apoptosis

To determine whether there are additional functional consequences of the statin-mediated mesenchymal shift in cell state, we performed kinetic live-cell imaging to observe cellular

(B) GSEA for cholesterol homeostasis of microarray data from ASPC1 cells treated with 5  $\mu$ M fluvastatin or control for 48 h.

(C) qRT-PCR of *HMGCR* expression in ASPC1 cells treated with 5  $\mu$ M fluvastatin, 0.5 mM MVA, or control, alone or in combination for 48 h; bar graphs indicate the mean, and error bars indicate  $\pm$  SEM of one representative out of three independent experiments. Significance test: one-way ANOVA.

(D) Mass spectrometry (MS) analysis for total cholesterol levels in ASPC1 cells treated as indicated in (C) for 48 h; bar graphs indicate the mean, and error bars indicate  $\pm$  SEM of three independent experiments.

(E) MS analysis for *de novo* cholesterol synthesis with  $^{13}$ C-labeled glucose of ASPC1 cells treated as indicated for 48 h; bar graphs indicate the mean, and error bars indicate  $\pm$  SEM of three independent experiments.

(F) GSEA for apoptosis gene set of microarray data from ASPC1 cells treated for 48 h with 5  $\mu$ M fluvastatin or control.

(G–I) Annexin V analysis of indicated cells after indicated treatment for 48 h; bar graphs indicate the mean, and error bars indicate  $\pm$  SEM of three independent experiments. Significance test: unpaired t test.

(J) GSEA for Kras signaling on microarray data from ASPC1 cells treated with 5  $\mu$ M fluvastatin or control for 48 h.

(K) Western blot for pERK (Thr202/Tyr204) and total ERK after indicated treatment for 48 h.

(L and N) Annexin V analysis after indicated treatment for 48 h; bar graphs indicate the mean, and error bars indicate  $\pm$  SEM of three independent experiments. Significance test: one-way ANOVA.

(M, O) Western blot for pERK (Thr202/Tyr204) and total ERK after indicated treatment for 48 h.

See also Figure S3 and Table S2.

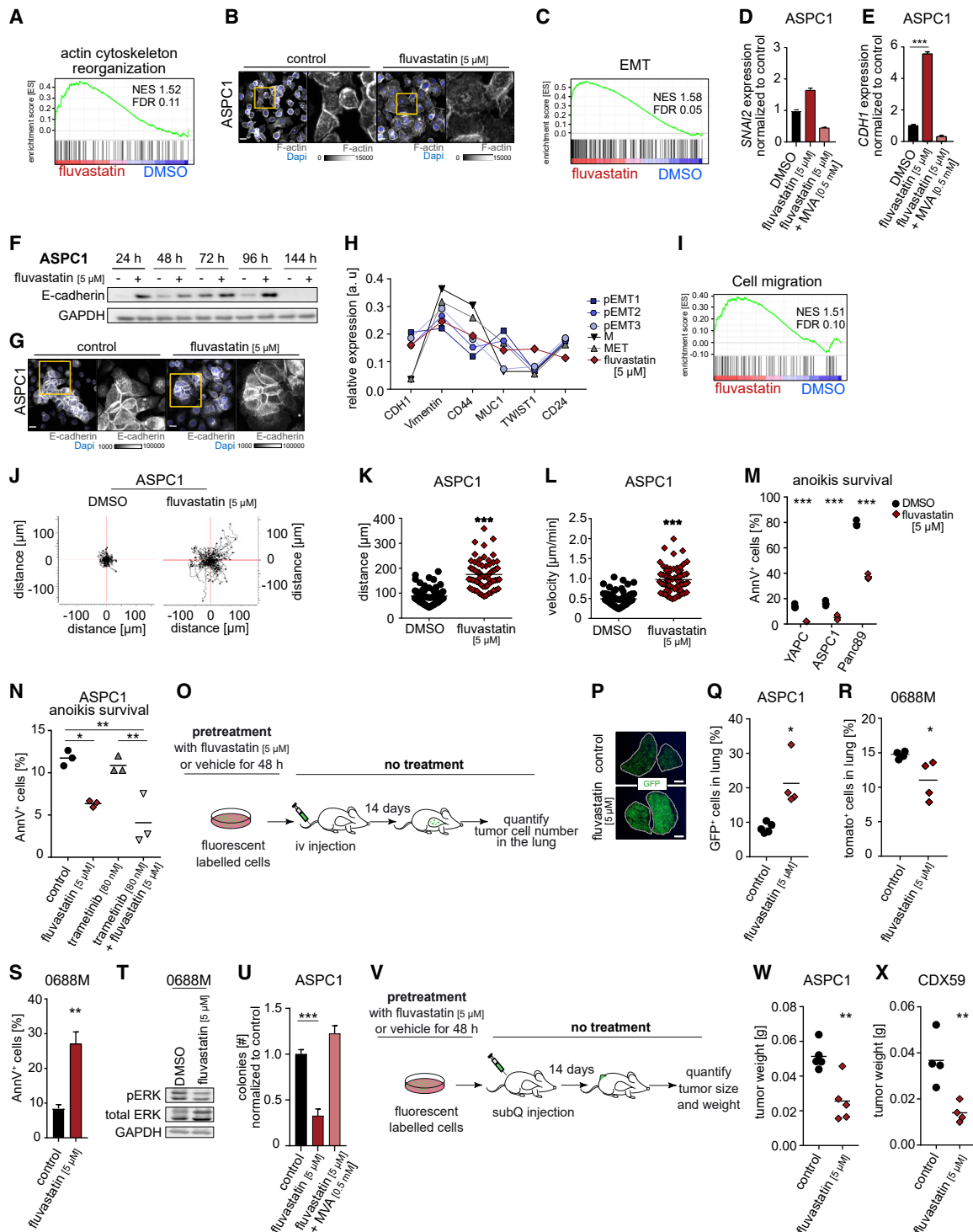


**Figure 4. Cholesterol pathway inhibition induces a partial EMT-like cell state and thereby inhibits tumor formation *in vivo***

(A) GSEA for actin cytoskeleton organization of microarray data from ASPC1 cells treated with 5  $\mu$ M fluvastatin or control for 48 h. (B) Representative confocal maximum projection and magnification (yellow boxes) of ASPC1 cells treated as indicated for 48 h; staining for rhodamine-phalloidin and DAPI (4',6-diamidino-2-phenylindole); scale bar: 20  $\mu$ m. (C) GSEA for EMT of microarray data from ASPC1 cells treated with 5  $\mu$ M fluvastatin or control for 48 h. (D and E) qRT-PCR of *SNAI2* (D) and *CDH1* (E) expression in ASPC1 cells treated as indicated for 48 h; bar graphs indicate the mean, and error bars indicate  $\pm$  SEM of one representative out of three independent experiments. Significance test: one-way ANOVA.

(legend continued on next page)

migratory capacity in statin- or vehicle-treated cells. Statin-treated cells exhibited an enhanced migratory capacity, with a significantly higher velocity and accumulated distance, accompanied by an upregulation of genes involved in migration (Figures 4I–4L and S5A–S5C). In addition, statin treatment actually increased resistance to anoikis (Figure 4M), a feature of mesenchymal cells enabling them to overcome the loss of cellular contacts (Simpson et al., 2008). Interestingly, the magnitude of anoikis resistance was again directly correlated with the magnitude of ERK activation and lack of apoptosis induction in the different cell lines (Figures 3G–3K). Additional ERK inhibition with the MEK inhibitor trametinib could not counteract the statin-induced resistance to anoikis (Figure 4N), indicating an exclusive effect of ERK-activation on escaping the induction of apoptosis. Survival in the bloodstream, which is a requirement for hematogenic spread (Piskounova et al., 2015; Elia et al., 2018), is characterized by resistance to anoikis and oxidative stress and is typically associated with a mesenchymal-like phenotype (Massagué and Obenauf, 2016; Steeg, 2006; Fares et al., 2020). To link our *in vitro* results on fluvastatin-induced cell motility to metastatic ability, GFP-labeled ASPC1 cells or YAPC cells were pretreated with fluvastatin or vehicle for 48 h and injected intravenously into recipient mice to evaluate the effects of statin treatment on survival in the bloodstream and ability to seed metastases in the lung (Figure 4O). In this model, cells have to stay alive in the bloodstream and resist oxidative stress and anoikis induction for several days before they enter the lung parenchyma and start to form secondary tumors, as was determined previously (Grüner et al., 2016). Pretreatment with fluvastatin increased the number of ASPC1 cells in the lungs after 14 days, and a similar effect was observed in YAPC cells (Figures 4P, 4Q, and S5D). To examine whether metastatic seeding ability correlates with apoptosis levels, we used mouse 0688M cells used in the initial screen and H1975 lung cancer cells, of which both present a high apoptotic rate and no increase in ERK acti-

vation upon fluvastatin treatment. Indeed, 0688M and H1975 cells showed reduced efficiency in metastatic seeding to the lung when pretreated with fluvastatin (Figures 4R–4T and S5E–S5G).

### Cholesterol-pathway inhibition reduces cellular plasticity and inhibits tumor and metastasis formation *in vivo*

The concept that cancer cells need to undergo EMT in order to metastasize and that mesenchymal cancer cells are more metastatic is broadly known (Massagué and Obenauf, 2016; Steeg, 2006; Fares et al., 2020). However, several studies have shown reduced metastatic ability in cancer cells subjected to statin treatment (Beckwitt et al., 2018; Yang et al., 2017). We confirmed these findings in mice, showing that established tumors develop fewer metastases when the mice are treated with statins (Figures 1F–1H). A closer look at our data points to a resolution of these initially counterintuitive findings. We hypothesized that the statin-induced cellular state leads to a reduction in cellular plasticity that plays a significant role in the metastatic transition of a cancer cell, as the cancer cells need to revert back to an epithelial phenotype once they have reached the secondary site in order to form metastases. Indeed, cancer cells that were treated with statins showed a significant reduction in colony formation, and this effect was even more pronounced when the cells were additionally pretreated with statins before seeding (Figures 4U and S5H–S5M). This result suggests that the reversion back to an epithelial state (including growth in a cellular cluster) (Massagué and Obenauf, 2016; Steeg, 2006; Fares et al., 2020) is suppressed under statin treatment.

To validate that MET is an important step for the successful generation of metastases affected by statin treatment *in vivo*, we pretreated GFP-labeled cancer cells with fluvastatin to induce a mesenchymal shift and analyzed the tumor-forming ability of cells by measuring the tumor weight and size of

(F) Western blot for E-cadherin in ASPC1 cells treated as indicated.

(G) Representative confocal sum projection and magnification (yellow boxes) of ASPC1 cells treated as indicated for 48 h. Cells were immunostained for E-cadherin and DAPI; scale bars: 20  $\mu$ m.

(H) Projected cell states of microarray data from ASPC1 cells treated as indicated for 48 h compared to bioinformatic analysis of Karacosta et al. (2019).

(I) GSEA for cell migration of microarray data from ASPC1 cells treated with 5  $\mu$ M fluvastatin or control for 48 h.

(J–L) Live-cell phase contrast imaging of ASPC1 cells. Quantification of migration velocity ( $\mu$ m/min) (L) and accumulated distance ( $\mu$ m) (K) from manual tracking shown in (J); n = 59–61 cells. Significance test: unpaired t test.

(M) Anoikis survival assay after 24 h with 48 h pretreatment as indicated from one representative out of three independent experiments; significance test: two-way ANOVA.

(N) Anoikis survival assay after 24 h with 48 h pretreatment as indicated from one representative out of three independent experiments; significance test: one-way ANOVA.

(O) Schematic of the *in vivo* experimental setup for intravenous injection to ascertain survival in the blood stream.

(P) Representative fluorescent image of lung lobes of mice intravenously injected with ASPC1-GFP cells pretreated as depicted in (O); scale bars: 1,000  $\mu$ m.

(Q and R) Number of cells in the lungs of mice intravenously injected and pretreated as depicted in (O); quantified by FACS as [%] of total lung cells; each dot represents a mouse, and the black line is the mean; n = 4–5 mice per group. Significance test: Mann-Whitney test.

(S) Annexin V analysis of 0688M cells with 48 h pretreatment as indicated; bar graphs indicate the mean, and error bars indicate  $\pm$  SEM of three independent experiments. Significance test: unpaired t test.

(T) Western blot for pERK (Thr202/Tyr204) and total ERK in 0688M cells treated as indicated for 48 h.

(U) Colony formation assay of ASPC1 cells pretreated for 48 h and with constant treatment during colony formation; bar graphs indicate the mean, and error bars indicate  $\pm$  SEM of three independent experiments. Significance test: Mann-Whitney test.

(V) Schematic of the *in vivo* experimental setup for subcutaneous injection to ascertain tumor formation.

(W and X) Tumor weight of subcutaneous tumors in mice injected with cells pretreated as depicted in (V); each dot represents a mouse, and the black line is the mean; n = 4–5 mice per group. Significance test: Mann-Whitney test.

See also Figures S4–S6.

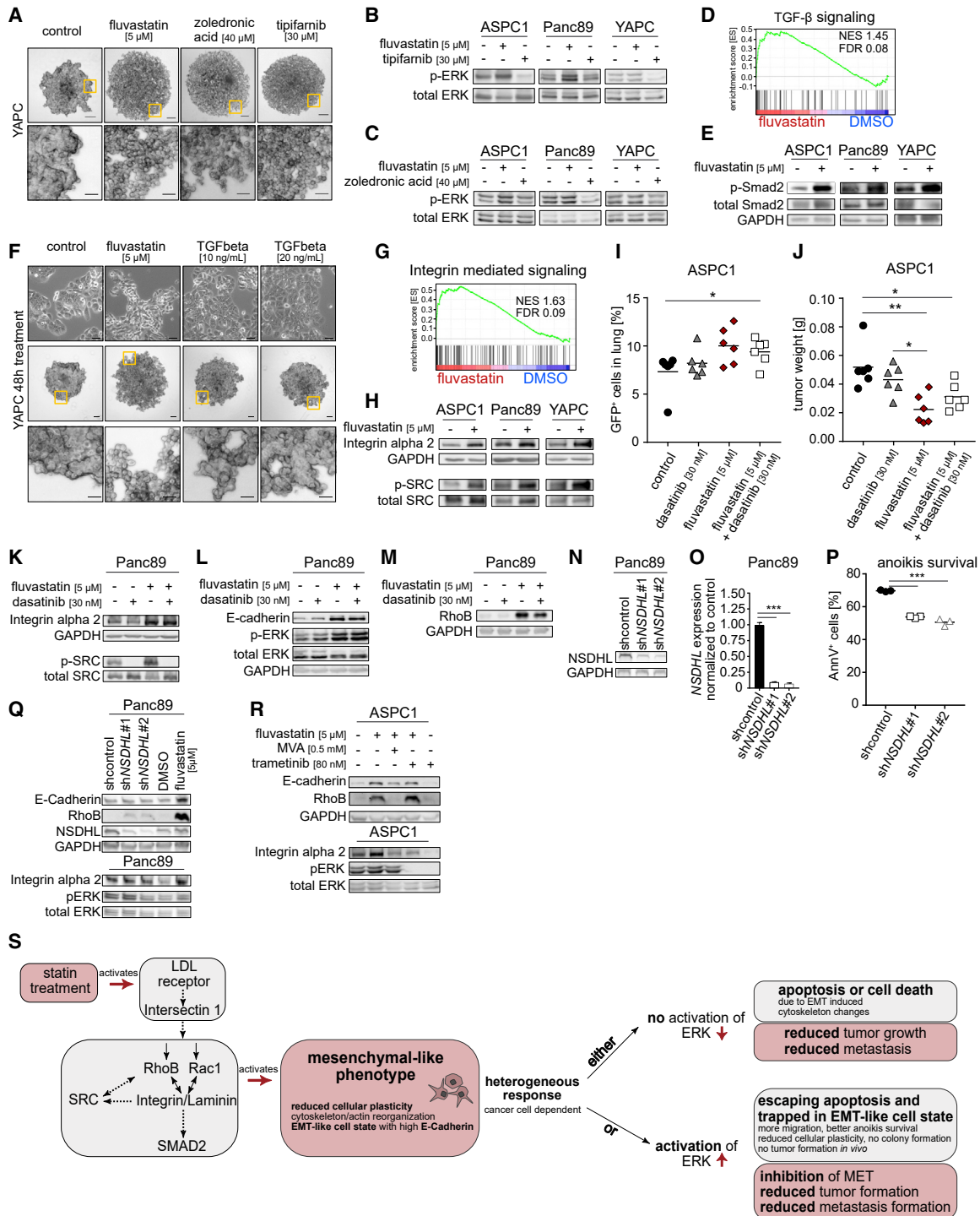


**Figure 5. Statin-induced morphodynamic changes are mediated by Rho-GTPases and Integrin signaling**

(A) Sphere formation of YAPC cells with 48 h pretreatment as indicated; yellow boxes: area chosen for magnification below. Scale bar: 75  $\mu$ m (top panel), 20  $\mu$ m (bottom panel).

(B and C) Western blot for pERK (Thr202/Tyr204) and total ERK after treatment as indicated for 48 h.

(D) GSEA for TGF- $\beta$  signaling of microarray data from ASPC1 cells treated with 5  $\mu$ M fluvastatin or control for 48 h.

(E) Western blot for pSMAD2 (Ser465/467) and total SMAD2 treated as indicated for 48 h.

(F) Top panel: YAPC cells in 2D cell culture after 48 h of treatment as indicated. Middle panel: Sphere formation of YAPC cells with pretreatment for 48 h as indicated; yellow boxes: area chosen for magnification below (bottom panel). Scale bar: 50  $\mu$ m (top and middle panel) and 20  $\mu$ m (bottom panel).

(legend continued on next page)

subcutaneous tumors after injection (Figure 4V). In this model, cells can directly start tumor formation upon injection, as in contrast to the intravenous injection model, no further barriers for establishing epithelial cell clusters and growth have to be overcome. Subcutaneous tumor size and weight were significantly reduced when ASPC1-GFP, YAPC-GFP, Panc89-GFP, or a PDAC-patient-derived cell line (CDX59-GFP) were pretreated with fluvastatin (Figures 4W, 4X, and S5N–S5S). Neither proliferation nor expression of E-Cadherin or Vimentin were different in the tumors that eventually formed, further emphasizing that only initial tumor formation is inhibited as long as statin-treatment is in effect (Figures S6A–S6D). Tumor growth, once the effect of statin treatment ceases, is not further affected, as also observed on molecular levels *in vitro*. Here, statin pretreatment and continuous ongoing treatment for 14 days were needed to uphold the effects on cellular signaling (Figures S6E and S6F). The effect on tumor formation could also not be rescued by the addition of Matrigel (Figures S6G and S6H). Thus, statin-mediated inhibition of tumor formation is independent of an apoptotic or proliferative response and Matrigel-mediated extracellular signaling.

#### Integrin and Rho-GTPase signaling induce statin-mediated reduction in phenotypic plasticity

Next, we investigated which cellular pathways mediate the statin-induced shift in cell state. Previous studies suggested statin-induced effects on metastatic cancer cells are due to an inhibition of prenylation downstream of the cholesterol biosynthesis pathway (Alizadeh et al., 2017; Gbelcová et al., 2017a). Yet, even though they induced alteration of cellular morphology comparable to that caused by statins (Figures 5A, S7A, and S7B), neither zoledronic acid, an inhibitor of farnesylpyrophosphate synthase, nor the farnesyl transferase inhibitor tipifarnib, caused increased levels of phosphorylated ERK (Figures 5B and 5C). Furthermore, zoledronic acid or tipifarnib pretreatment did not increase *in vivo* metastatic seeding ability in ASPC1 or Panc89 cells when tested in our metastatic seeding platform; rather, seeding ability decreased as expected, indicating a distinct mechanism of action and effect on cellular signaling from the statin drug class (Figures S7C and S7D).

Similarly, GSEA analysis revealed that transforming growth factor  $\beta$  (TGF- $\beta$ ) signaling was upregulated in statin-treated cancer cells, which was accompanied by increased SMAD2 phosphorylation (Figures 5D and 5E). However, treatment with recombinant TGF- $\beta$  could not recapitulate the statin-induced cellular phenotype in sphere culture or the statin-induced molecular changes in signaling, indicating that TGF- $\beta$  signaling is a consequence rather than cause of the observed cell state shift (Figures 5F and S7E–S7G).

Of note, GSEA also suggested upregulation of integrin signaling upon statin treatment, which involved Rho proteins, laminins, Integrin alpha 2, and SRC (Figures 3A, 5G, and 5H). SRC activation has already been described to induce various morphodynamic changes by integrin signaling, which reportedly also induces EMT (Huvneers and Danen, 2009; Zhang et al., 2017; Desgrosellier and Cheresch, 2010). Therefore, we determined whether SRC inhibition by dasatinib treatment could revert the fluvastatin-induced phenotypes. Dasatinib treatment only partially rescued the statin-induced changes in 3D sphere culture (Figures S7H and S7I) and upon intravenous or subcutaneous injection *in vivo* (Figures 5I, 5J, and S7J). Yet, dasatinib treatment was unable to revert statin-induced increases in E-cadherin and Integrin alpha 2, demonstrating that SRC activation might be a consequence of integrin signaling (Figures 5K, 5L, and S7K–S7P). Interestingly, statin-induced ERK and RhoB activation upon combinatorial treatment with dasatinib was cell line dependent (Figures 5L, 5M, and S7M–S7P). These data indicate that the fluvastatin-mediated effect on phenotypic cell state (and consequently tumor formation) is only partially dependent on SRC activation. As dasatinib can have other targets besides SRC (Olivieri and Manzione, 2007), it is possible that they—rather than SRC—might be the mediators of the statin effect. Similarly, as dasatinib only partially affects the *in vivo* phenotype of statin treatment, it is highly likely that a multilevel response maintains total cholesterol levels after statin-mediated inhibition of *de novo* cholesterol biosynthesis that in turn results in the mesenchymal phenotype. Indeed, genetic knockdown of NAD (P)-dependent steroid dehydrogenase-like (NSDHL), which is involved in the sterol biosynthesis pathway downstream of HMGCR (Wilcox et al., 2007; Gabitova-Cornell et al., 2020),

(G) GSEA for Integrin-mediated signaling of microarray data from ASPC1 cells treated for 48 h with 5  $\mu$ M fluvastatin or control.

(H) Western blot for pSRC (Tyr416), total SRC, and Integrin alpha 2 after treatment as indicated for 48 h.

(I) Number of cells in the lungs of mice intravenously injected with ASPC1-GFP cells pretreated as depicted in (Figure 4O); quantified by FACS as [%] of total lung cells; each dot represents a mouse, and the black line is the mean;  $n = 5$  mice per group. Significance test: Mann-Whitney test.

(J) Tumor weight of subcutaneous tumors in mice injected with ASPC1-GFP cells pretreated as depicted in (Figure 4V); each dot represents a mouse, and the black line is the mean;  $n = 5$  mice per group. Significance test: Mann-Whitney test.

(K–M) Western blot for pSRC (Tyr416), total SRC, Integrin alpha 2, phospho-ERK (Thr202/Tyr204), total ERK, E-cadherin, and RhoB in Panc89 cells treated for 48 h as indicated.

(N) Western blot for NSDHL in Panc89 shcontrol, shNSDHL#1, and shNSDHL#2 cells.

(O) qRT-PCR of NSDHL in Panc89 shcontrol, shNSDHL#1, and shNSDHL#2 cells; bar graphs indicate the mean, and error bars indicate  $\pm$  SEM of one representative out of three independent experiments. Significance test: one-way ANOVA.

(P) Anoikis survival assay of Panc89 shcontrol, shNSDHL#1, and shNSDHL#2 cells after 24 h from one representative out of three independent experiments; significance test: ANOVA.

(Q) Western blot for Integrin alpha 2, pERK (Thr202/Tyr204), total ERK, E-cadherin, and RhoB in Panc89 cells treated for 48 h as indicated and Panc89 shcontrol, shNSDHL#1, and shNSDHL#2 cells.

(R) Western blot for Integrin alpha 2, pERK (Thr202/Tyr204), total ERK, E-cadherin, and RhoB in ASPC1 cells treated for 48 h as indicated.

(S) Schematic of morphological and signaling effects of statin treatment on PDAC cells. Dashed arrows indicate hypothesized; continuous arrows indicate data-based interactions.

See also Figures S7 and S8.

also partially phenocopies the statin-mediated effect. Morphological changes in *NSDHL* knockdown cells in 2D and in 3D sphere culture and enhanced anoikis survival capacity display the beginning of a mesenchymal phenotype, which is less prominent than that in statin-treated cells (Figure 5N–5P and S8A–S8E). On a molecular level, *NSDHL* knockdown results in a slight induction of Integrin alpha 2, E-Cadherin, and RhoB (Figures 5Q and S8F) that was partly cell line dependent. The lesser effect of *NSDHL* knockdown than statin treatment might be due to a compensatory effect that takes place during the selection process in the knockdown cells that acute pharmacological inhibition does not cause, or it may display the more prominent role of HMGCR as a rate-limiting enzyme during cholesterol biosynthesis.

It was shown previously that ectopic expression of HRAS induced EMT and sensitized cells to statin treatment (Yu et al., 2018). In our study, cells with no change or low levels of pERK after fluvastatin treatment (YAPC, 0688M, and H1975) still upregulated RhoB, E-cadherin, and Integrin alpha 2 (Figures S7K, S7M, S7O, S8G, and S8H). In contrast, in cells that activate ERK upon statin treatment, trametinib treatment could not counteract the activation of RhoB, Integrin alpha 2, and E-cadherin (Figure 5R). This finding is independent of the cell state subtype of the pancreatic cancer cells, as statin treatment induced a mesenchymal morphology shift in the classical PDAC cells (PA-TU-8988S) and demonstrated similar effects on both classical (PA-TU-8988S) and QM (quasi-mesenchymal)/basal cells (PA-TU-8988T) on functional and molecular levels, suggesting a general effect on cellular signaling but inducing morphology changes only in cells that do not yet present with a mesenchymal phenotype (Figures S8I–S8L). This result further endorses the conclusion that the activation of ERK is independent of the induction of the EMT-like phenotype and is a consequence of the cell state change to counteract the induction of apoptosis. The cells' intrinsic capability to activate ERK determines the treatment outcome. Cells that are unable to undergo statin-induced EMT become apoptotic, a well-known concept in tissue homeostasis, turnover, and EMT-mediated disruption of lineage-specific transcriptional networks (Flusberg and Sorger, 2015; David et al., 2016).

In addition, it is known that unligated integrins on adherent cells can induce apoptosis by recruiting and activating caspase 8 (Zhao et al., 2005; Frisch and Screaton, 2001). Therefore, we speculate that the mesenchymal-like cell state shift, during which cancer cells lose their contacts to each other, is accompanied by the upregulation of several integrins, promoting an apoptotic phenotype. Cells that then have the capacity for ERK activation can counteract this induction of apoptosis but are still trapped in their mesenchymal phenotype.

Taken together, our study demonstrates that the inhibition of the intracellular cholesterol biosynthesis and the multilevel counter mechanisms of the cells to maintain cholesterol levels induce an EMT-like cell state through upregulation of multiple integrins and laminins, likely through activation of ITSN1. Integrins then likely activate Rho-family proteins that in turn can activate SRC and TGF- $\beta$  signaling to induce and maintain this mesenchymal state, potentially involving positive feedback loops (Desgrosellier and Cheresh, 2010). As a conse-

quence of this shift in cell state, statin treatment traps cancer cells in a mesenchymal-like state, effectively reducing their cellular plasticity. Once cells enter this mesenchymal-like state, upregulation of ERK activity counteracts apoptotic programs. Although the reduced metastatic ability of statin-treated cells that are unable to activate ERK (i.e., 0688M or H1975) seems readily explainable, cancer cells capable of ERK activation (i.e., ASPC1 or Panc89) have increased metastatic seeding ability driven by enhanced migration, extravasation, and survival in the bloodstream. However, the statin-induced mesenchymal cell state shift renders the cancer cells unable to undergo MET, ultimately inhibiting their cellular plasticity and therefore inhibiting their ability to form metastatic colonies (summarized in Figure 5S).

## DISCUSSION

During 2003–2012, the overall use of statins increased from 18% to 26% in adult patients over the age of 40, with upward tendency. Furthermore, the US guidelines regarding cholesterol levels and statin use were updated in 2013, causing an additional increase in statin use (Stone et al., 2014). Cholesterol-lowering medication use increases with age, from 17% of adults aged 40–59 to every 2nd adult above 75, of which more than 90% use statins (Gu et al., 2014). Even though the effect of drugs on other drugs (drug-drug interactions) and also on other diseases besides the one for which they are prescribed (drug-disease interactions) is well acknowledged, the number of studies addressing these interactions is limited (Hanlon et al., 2017; Campen et al., 2017). Therefore, it is of utmost importance to understand the impact of statin medication on cancer patients, not only tumor formation and progression but also on cancer metastasis and treatment response.

The effect of statins as a potential treatment for cancer development, progression, and metastasis has been the subject of many preclinical and clinical studies (Iannelli et al., 2018; Farooqi et al., 2018; Huang et al., 2016). Yet, even for patients who are on statins to treat their hypercholesterolemia, it is important for clinicians to know what this treatment may do to their cancer disease. Here, we show that statin treatment directly induces EMT and thereby reduces cell plasticity. In other studies, statin treatment was suggested to inhibit rather than induce EMT of several different cancer types, which was indicated in part by the upregulation of epithelial markers like E-cadherin (Xie et al., 2016; Kato et al., 2018; Koohestanimobarhan et al., 2018). Importantly, we also observed an upregulation of E-cadherin upon statin treatment. Yet, in our study, this result was accompanied by phenotypic and molecular changes toward a mesenchymal phenotype in which the cancer cells are trapped as long as statins are present, preventing them from undergoing MET transition and metastasis formation. In addition, relative E-cadherin expression levels were still in accordance with a partial EMT state that was previously defined for lung cancer (Karcosta et al., 2019). Whether E-cadherin upregulation is functional or a mechanism to counteract the induced mesenchymal cell shift remains unclear. Similarly, Porter et al. (2019) demonstrated that FOLFIRINOX combination chemotherapy induces a shift of PDAC subtypes toward a more QM/basal state, whereas vitamin

D induces distinct transcriptional responses in each subtype that lead to differential responses on tumor progression and metastasis.

Recently, cholesterol pathway inhibition was suggested to induce EMT in primary PDAC tumors, resulting in dedifferentiation to the basal subtype (Gabitova-Cornell et al., 2020). Although a statin-induced mesenchymal phenotype is less favorable for primary PDAC, our study shows that it also prevents PDAC metastasis so long as it can be sustained and the required cellular plasticity to perform MET is inhibited. Thus, the time point of EMT induction during cancer development, progression, and metastasis determines its outcome. Indeed, in the background of the autochthonous KPC model for pancreatic cancer, mice with additional *NSDHL* deficiency, which causes disrupted cholesterol biosynthesis, live longer and develop less frequent PDAC (Gabitova-Cornell et al., 2020). In line with this finding, knockdown of *NSDHL* partially phenocopied the effects of statin treatment in our study, indicating similar effects on tumor and metastasis formation. In the study by Gabitova-Cornell et al. (2020), this result was attributed to the induction of apoptosis upon EMT-mediated disruption of lineage-specific transcriptional networks, as was described previously (David et al., 2016). In those mice, PDAC developed only when there was enough oncogenic pressure to increase plasticity. This finding is conceptually similar to the results of our study, in which cancer cells could overcome apoptosis by upregulating ERK signaling. Thus, our findings emphasize that targeted therapies can have opposing effects on primary tumor and metastases formation in comparison to tumor progression, underscoring the importance of proper timing of anti-cancer therapies and the distinct effects that inhibition of plasticity can have on different stages of tumor development and progression. Indeed, our data suggest that the development of resistance or discontinuation of statin treatment in cancer patients could promote PDAC metastasis and emphasize the complexity of cholesterol biology in terms of tumor progression.

Consistent with our findings, several retrospective studies support a positive outcome for cancer patients who take statins to treat their hypercholesterolemia. Several large clinical trials revealed that statin treatment reduces the risk to develop PDAC by up to 30% (Archibugi et al., 2019). Furthermore, statin treatment correlates with a reduced risk of death in resected PDAC patients but not in those with advanced disease (Zhang et al., 2019b; Archibugi et al., 2019; Tamburrino et al., 2020; Abdel-Rahman, 2019; Archibugi et al., 2017; Farooqi et al., 2018; Walker et al., 2015). Interestingly, a recent retrospective analysis of data from over 2,000 PDAC patients revealed that the positive effects of statin treatment on mortality are independent from their effect on cholesterol levels (Huang et al., 2016). In our study, we observed that overall cholesterol levels remain unchanged upon statin treatment. Thus, these clinical data are entirely consistent with our molecular and cellular findings. Although the concentrations used here do not completely correspond with the concentrations generally used for patient treatment—treatment doses of 0.1–1 mg/kg and serum levels of approximately 10 nM (Björkhem-Bergman et al., 2011)—they are in general in concordance with concentrations used in preclinical studies and did not induce any adverse effects (Baek et al.,

2017; Beckwitt et al., 2018; Hoque et al., 2008). Noteworthy, statins also affect other cells in the human body, such as immune cells. Baek et al. (2017) could show that cholesterol promotes breast cancer metastasis by its metabolite 27-hydroxycholesterol (27HC) that acts on immune myeloid cells residing at the distal metastatic sites, thus promoting an immune suppressive environment. Another study demonstrated that perturbed cholesterol homeostasis leads to an EMT-like state in breast cancer cells, promoting metastasis by affecting both cancer cells and tumor-associated macrophages (Nelson et al., 2013).

Our results suggest that the clinical benefit of statin treatment in early diagnosed or resected cancer patients could be driven by a reduction in the formation of new metastases due to inhibition of MET. In addition, the statin-induced mesenchymal cell state is reversible and persists only as long as statins are present. From a therapeutic standpoint, it is important that chronic statin treatment is generally well-tolerated in patients even at high doses (De Angelis, 2004), even though they can cause myopathy as most common off-target effect due to inhibition of mitochondria complex III by the lactone form of statins (Schirris et al., 2015). In addition, beneficial off-target effects of statins have been described, although the causes are still unclear, including improved endothelial function, increased plaque stability, antithrombotic and anti-inflammatory effects, reduced risk of dementia and Alzheimer disease, and reduced ischemic stroke (Murphy et al., 2020). Therefore, this class of drugs is well-suited for continuous therapy, which would be required to block the development of metastases in patients with resected tumors or early metastasis.

#### Limitations of the study

One limitation of our study is certainly that the exact timing of statin-mediated effects in patients is still not completely clear. Whether or not the exact effects on tumors and metastases are the same at the onset of the disease or with established tumors would need to be determined in controlled prospective clinical studies. In addition, the exact molecular links that connect cholesterol levels and distribution with cellular signaling are yet to be determined.

#### STAR★METHODS

Detailed methods are provided in the online version of this paper and include the following:

- KEY RESOURCES TABLE
- RESOURCE AVAILABILITY
  - Lead contact
  - Materials availability
  - Data and code availability
- EXPERIMENTAL MODEL AND SUBJECT DETAILS
  - *In vivo* animal studies
  - Cell lines and primary cultures
- METHOD DETAILS
  - Generation of PDX derived cell line (CDX 59)
  - Chemicals
  - Viral transduction of cells
  - Immunofluorescence (Actin and E-cadherin staining)

- Live cell imaging and live cell tracking
- <sup>13</sup>C-labeling experiments
- Spheroid formation assay
- Assessment of *in vitro* viability
- Annexin V staining
- Anoikis survival assay
- Cell cycle analysis
- Colony formation assay
- Microarray analysis
- Gene set enrichment analysis
- Proteome and phosphorylated proteome analysis
- STRING analysis
- EMT-States comparison analysis
- Western Blot
- Quantitative real-time PCR (qRT-PCR)
- *In vivo* experiments
- Histology and immunohistochemistry
- **QUANTIFICATION AND STATISTICAL ANALYSIS**

#### SUPPLEMENTAL INFORMATION

Supplemental information can be found online at <https://doi.org/10.1016/j.celrep.2021.110056>.

#### ACKNOWLEDGMENTS

We thank Eva Hahn, the Stanford High-Throughput Bioscience Center, and the Central animal facility of the University Hospital Duisburg-Essen for technical support. This work was funded by the Deutsche Forschungsgemeinschaft (DFG, German Research Foundation) with an Emmy Noether Award (GR4575/1-1 to B.M.G.) and by SFB1430 project-ID 424228829 (to B.M.G., P.N., M. Kaiser, and F.K.). P.D. is a recipient of a PhD fellowship from Cusanuswerk. S.-M.F. acknowledges funding from the European Research Council under the ERC Consolidator Grant Agreement no. 771486–MetaRegulation, FWO – Research Projects, King Baudouin foundation funding, and Fonds Baillet Latour. This work was supported by the DFG (INST 20876/322-1 FUGG to M. Kaiser and F.K.). A.S. acknowledges funding from the DFG as part of the SFB 876, TP C1. J.T.S. is supported by the German Cancer Consortium (DKTK), the DFG through grant SI1549/3-1 (Clinical Research Unit KFO337) and SI1549/4-1, the German Cancer Aid (70112505/PIPAC and 70113834/PREDICT-PACA), and the Wilhelm Sander-Stiftung (2019.008.1)

#### AUTHOR CONTRIBUTIONS

Conceptualization, B.M.G., M.M.W., and M.D.; methodology, B.M.G. and M.D.; validation, M.D. and S.U.; formal analysis, M.D., M. Kowalczyk, J.F., S.O., G.H., and F.K.; investigation, M.D., M. Kowalczyk, M.P., S.U., K.U., P.D., S.N., G.H., F.K., and A.P.; resources, S.T.L., F.K., M. Kaiser, J.T.S., A.S., M.M.W., S.-M.F., and P.N.; writing – original draft, M.D. and B.M.G.; writing – review & editing, M.D., S.T.L., F.K., M. Kaiser, J.T.S., A.S., M.M.W., S.-M.F., P.N., and B.M.G.; visualization, B.M.G. and M.D.; funding acquisition, B.M.G.

#### DECLARATION OF INTERESTS

J.T.S. reports the following disclosures: Bristol-Myers Squibb, Celgene, and Roche (research funding); AstraZeneca, Bristol-Myers Squibb, Celgene, Immunocore, Novartis, Roche, and Shire (consulting or advisory role); AstraZeneca, Aurikamed, Baxalta, Bristol Myers Squibb, Celgene, Falk Foundation, iomedico, Immunocore, Novartis, Roche, and Shire (honoraria); and minor equity in iTheragnostics and Pharma15 (<3%) and member of the Board of Directors for Pharma15, all outside the submitted work. All other authors declare no competing interests.

Received: April 30, 2021  
Revised: September 21, 2021  
Accepted: November 3, 2021  
Published: November 23, 2021

#### REFERENCES

- Abdel-Rahman, O. (2019). Statin treatment and outcomes of metastatic pancreatic cancer: a pooled analysis of two phase III studies. *Clin. Transl. Oncol.* *21*, 810–816.
- Alizadeh, J., Zeki, A.A., Mirzaei, N., Tewary, S., Rezaei Moghadam, A., Glogowska, A., Nagakannan, P., Eftekharpour, E., Wiechec, E., Gordon, J.W., et al. (2017). Mevalonate Cascade Inhibition by Simvastatin Induces the Intrinsic Apoptosis Pathway via Depletion of Isoprenoids in Tumor Cells. *Sci. Rep.* *7*, 44841.
- Archibugi, L., Piciucchi, M., Stigliano, S., Valente, R., Zerboni, G., Barucca, V., Milella, M., Maisonneuve, P., Delle Fave, G., and Capurso, G. (2017). Exclusive and Combined Use of Statins and Aspirin and the Risk of Pancreatic Cancer: a Case-Control Study. *Sci. Rep.* *7*, 13024.
- Archibugi, L., Arcidiacono, P.G., and Capurso, G. (2019). Statin use is associated to a reduced risk of pancreatic cancer: A meta-analysis. *Dig. Liver Dis.* *51*, 28–37.
- Baek, A.E., Yu, Y.A., He, S., Wardell, S.E., Chang, C.Y., Kwon, S., Pillai, R.V., McDowell, H.B., Thompson, J.W., Dubois, L.G., et al. (2017). The cholesterol metabolite 27 hydroxycholesterol facilitates breast cancer metastasis through its actions on immune cells. *Nat. Commun.* *8*, 864.
- Beckwitt, C.H., Clark, A.M., Ma, B., Whaley, D., Oltvai, Z.N., and Wells, A. (2018). Statins attenuate outgrowth of breast cancer metastases. *Br. J. Cancer* *119*, 1094–1105.
- Bjarnadottir, O., Romero, Q., Bendahl, P.O., Jirström, K., Rydén, L., Loman, N., Uhlén, M., Johannesson, H., Rose, C., Grabau, D., and Borgquist, S. (2013). Targeting HMG-CoA reductase with statins in a window-of-opportunity breast cancer trial. *Breast Cancer Res. Treat.* *138*, 499–508.
- Björkhem-Bergman, L., Lindh, J.D., and Bergman, P. (2011). What is a relevant statin concentration in cell experiments claiming pleiotropic effects? *Br. J. Clin. Pharmacol.* *72*, 164–165.
- Brown, M.S., and Goldstein, J.L. (1980). Multivalent feedback regulation of HMG CoA reductase, a control mechanism coordinating isoprenoid synthesis and cell growth. *J. Lipid Res.* *21*, 505–517.
- Bukholm, I.K., Nesland, J.M., and Børresen-Dale, A.L. (2000). Re-expression of E-cadherin, alpha-catenin and beta-catenin, but not of gamma-catenin, in metastatic tissue from breast cancer patients [see comments]. *J. Pathol.* *190*, 15–19.
- Campan, C.J., Vogel, W.H., and Shah, P.J. (2017). Managing Drug Interactions in Cancer Therapy: A Guide for the Advanced Practitioner. *J. Adv. Pract. Oncol.* *8*, 609–620.
- Cox, J., and Mann, M. (2008). MaxQuant enables high peptide identification rates, individualized p.p.b.-range mass accuracies and proteome-wide protein quantification. *Nat. Biotechnol.* *26*, 1367–1372.
- Cox, J., Neuhauser, N., Michalski, A., Scheltema, R.A., Olsen, J.V., and Mann, M. (2011). Andromeda: a peptide search engine integrated into the MaxQuant environment. *J. Proteome Res.* *10*, 1794–1805.
- Cox, J., Hein, M.Y., Lubner, C.A., Paron, I., Nagaraj, N., and Mann, M. (2014). Accurate proteome-wide label-free quantification by delayed normalization and maximal peptide ratio extraction, termed MaxLFQ. *Mol. Cell. Proteomics* *13*, 2513–2526.
- David, C.J., Huang, Y.H., Chen, M., Su, J., Zou, Y., Bardeesy, N., Iacobuzio-Donahue, C.A., and Massagué, J. (2016). TGF- $\beta$  Tumor Suppression through a Lethal EMT. *Cell* *164*, 1015–1030.
- De Angelis, G. (2004). The influence of statin characteristics on their safety and tolerability. *Int. J. Clin. Pract.* *58*, 945–955.
- Desgrosellier, J.S., and Cheresch, D.A. (2010). Integrins in cancer: biological implications and therapeutic opportunities. *Nat. Rev. Cancer* *10*, 9–22.

- Elia, I., Broekaert, D., Christen, S., Boon, R., Radaelli, E., Orth, M.F., Verfaillie, C., Grünwald, T.G.P., and Fendt, S.M. (2017). Proline metabolism supports metastasis formation and could be inhibited to selectively target metastasizing cancer cells. *Nat. Commun.* **8**, 15267.
- Elia, I., Doglioni, G., and Fendt, S.M. (2018). Metabolic Hallmarks of Metastasis Formation. *Trends Cell Biol.* **28**, 673–684.
- Fares, J., Fares, M.Y., Khachfe, H.H., Salhab, H.A., and Fares, Y. (2020). Molecular principles of metastasis: a hallmark of cancer revisited. *Signal Transduct. Target. Ther.* **5**, 28.
- Farooqi, M.A.M., Malhotra, N., Mukherjee, S.D., Sanger, S., Dhesy-Thind, S.K., Ellis, P., and Leong, D.P. (2018). Statin therapy in the treatment of active cancer: A systematic review and meta-analysis of randomized controlled trials. *PLoS One* **13**, e0209486.
- Fernandez, C.A., Des Rosiers, C., Previs, S.F., David, F., and Brunengraber, H. (1996). Correction of 13C mass isotopomer distributions for natural stable isotope abundance. *J. Mass Spectrom.* **31**, 255–262.
- Flusberg, D.A., and Sorger, P.K. (2015). Surviving apoptosis: life-death signaling in single cells. *Trends Cell Biol.* **25**, 446–458.
- Frisch, S.M., and Screaton, R.A. (2001). Anoikis mechanisms. *Curr. Opin. Cell Biol.* **13**, 555–562.
- Gabitova-Cornell, L., Surumbayeva, A., Peri, S., Franco-Barraza, J., Restifo, D., Weitz, N., Ogier, C., Goldman, A.R., Hartman, T.R., Francescone, R., et al. (2020). Cholesterol Pathway Inhibition Induces TGF- $\beta$  Signaling to Promote Basal Differentiation in Pancreatic Cancer. *Cancer Cell* **38**, 567–583.e11.
- Gbelcová, H., Leníček, M., Zelenka, J., Knejzlík, Z., Dvoráková, G., Zadinová, M., Poucková, P., Kudla, M., Balaz, P., Ruml, T., and Vítek, L. (2008). Differences in antitumor effects of various statins on human pancreatic cancer. *Int. J. Cancer* **122**, 1214–1221.
- Gbelcová, H., Rimpelová, S., Knejzlík, Z., Šáchová, J., Kolář, M., Strnad, H., Repiská, V., D'Acunto, W.C., Ruml, T., and Vítek, L. (2017a). Isoprenoids responsible for protein prenylation modulate the biological effects of statins on pancreatic cancer cells. *Lipids Health Dis.* **16**, 250.
- Gbelcová, H., Rimpelová, S., Ruml, T., Fenclová, M., Kosek, V., Hajšlová, J., Strnad, H., Kolář, M., and Vítek, L. (2017b). Variability in statin-induced changes in gene expression profiles of pancreatic cancer. *Sci. Rep.* **7**, 44219.
- Greenwood, J., Steinman, L., and Zamvil, S.S. (2006). Statin therapy and autoimmune disease: from protein prenylation to immunomodulation. *Nat. Rev. Immunol.* **6**, 358–370.
- Grüner, B.M., Schulze, C.J., Yang, D., Ogasawara, D., Dix, M.M., Rogers, Z.N., Chuang, C.H., McFarland, C.D., Chiou, S.H., Brown, J.M., et al. (2016). An in vivo multiplexed small-molecule screening platform. *Nat. Methods* **13**, 883–889.
- Gu, Q., Raulose-Ram, R., Burt, V.L., and Kit, B.K. (2014). Prescription cholesterol-lowering medication use in adults aged 40 and over: United States, 2003–2012. *NCHS Data Brief*, 1–8.
- Gupta, P.B., Pastushenko, I., Skibinski, A., Blanpain, C., and Kuperwasser, C. (2019). Phenotypic Plasticity: Driver of Cancer Initiation, Progression, and Therapy Resistance. *Cell Stem Cell* **24**, 65–78.
- Hanlon, J.T., Perera, S., Newman, A.B., Thorpe, J.M., Donohue, J.M., Simonick, E.M., Shorr, R.I., Bauer, D.C., and Marcum, Z.A.; Health ABC Study (2017). Potential drug-drug and drug-disease interactions in well-functioning community-dwelling older adults. *J. Clin. Pharm. Ther.* **42**, 228–233.
- Hollestelle, A., Peeters, J.K., Smid, M., Timmermans, M., Verhoog, L.C., Westendorp, P.J., Heine, A.A., Chan, A., Sieuwerts, A.M., Wiemer, E.A., et al. (2013). Loss of E-cadherin is not a necessity for epithelial to mesenchymal transition in human breast cancer. *Breast Cancer Res. Treat.* **138**, 47–57.
- Hoque, A., Chen, H., and Xu, X.C. (2008). Statin induces apoptosis and cell growth arrest in prostate cancer cells. *Cancer Epidemiol. Biomarkers Prev.* **17**, 88–94.
- Huang, B.Z., Chang, J.I., Li, E., Xiang, A.H., and Wu, B.U. (2016). Influence of Statins and Cholesterol on Mortality Among Patients With Pancreatic Cancer. *J. Natl. Cancer Inst.* **109**, djw275.
- Humphrey, S.J., Azimifar, S.B., and Mann, M. (2015). High-throughput phosphoproteomics reveals in vivo insulin signaling dynamics. *Nat. Biotechnol.* **33**, 990–995.
- Huvneers, S., and Danen, E.H. (2009). Adhesion signaling—crosstalk between integrins, Src and Rho. *J. Cell Sci.* **122**, 1059–1069.
- Iannelli, F., Lombardi, R., Milone, M.R., Pucci, B., De Rienzo, S., Budillon, A., and Bruzzese, F. (2018). Targeting Mevalonate Pathway in Cancer Treatment: Repurposing of Statins. *Recent Patents Anticancer Drug Discov.* **13**, 184–200.
- Karacosta, L.G., Anchang, B., Ignatiadis, N., Kimmey, S.C., Benson, J.A., Shrager, J.B., Tibshirani, R., Bendall, S.C., and Plevritis, S.K. (2019). Mapping lung cancer epithelial-mesenchymal transition states and trajectories with single-cell resolution. *Nat. Commun.* **10**, 5587.
- Kato, S., Liberona, M.F., Cerda-Infante, J., Sánchez, M., Henríquez, J., Bizama, C., Bravo, M.L., Gonzalez, P., Gejman, R., Brañes, J., et al. (2018). Simvastatin interferes with cancer 'stem-cell' plasticity reducing metastasis in ovarian cancer. *Endocr. Relat. Cancer* **25**, 821–836.
- Kharroubi, A.T., Masterson, T.M., Aldaghlis, T.A., Kennedy, K.A., and Kelleher, J.K. (1992). Isotopomer spectral analysis of triglyceride fatty acid synthesis in 3T3-L1 cells. *Am. J. Physiol.* **263**, E667–E675.
- Koohestanimobarhan, S., Salami, S., Imeni, V., Mohammadi, Z., and Bayat, O. (2018). Lipophilic statins antagonistically alter the major epithelial-to-mesenchymal transition signaling pathways in breast cancer stem-like cells via inhibition of the mevalonate pathway. *J. Cell. Biochem.* **120**, 2515–2531.
- Lorendeau, D., Rinaldi, G., Boon, R., Spincemaille, P., Metzger, K., Jäger, C., Christen, S., Dong, X., Kuenen, S., Voordeckers, K., et al. (2017). Dual loss of succinate dehydrogenase (SDH) and complex I activity is necessary to recapitulate the metabolic phenotype of SDH mutant tumors. *Metab. Eng.* **43**, 187–197.
- Luu, W., Sharpe, L.J., Gelissen, I.C., and Brown, A.J. (2013). The role of signaling in cellular cholesterol homeostasis. *IUBMB Life* **65**, 675–684.
- Massagué, J., and Obenauf, A.C. (2016). Metastatic colonization by circulating tumour cells. *Nature* **529**, 298–306.
- Mootha, V.K., Lindgren, C.M., Eriksson, K.F., Subramanian, A., Sihag, S., Lehar, J., Puigserver, P., Carlsson, E., Ridderstråle, M., Laurila, E., et al. (2003). PGC-1 $\alpha$ -responsive genes involved in oxidative phosphorylation are coordinately downregulated in human diabetes. *Nat. Genet.* **34**, 267–273.
- Murphy, C., Deplazes, E., Cranfield, C.G., and Garcia, A. (2020). The Role of Structure and Biophysical Properties in the Pleiotropic Effects of Statins. *Int. J. Mol. Sci.* **21**, 8745.
- Nelson, E.R., Wardell, S.E., Jasper, J.S., Park, S., Suchindran, S., Howe, M.K., Carver, N.J., Pillai, R.V., Sullivan, P.M., Sondhi, V., et al. (2013). 27-Hydroxycholesterol links hypercholesterolemia and breast cancer pathophysiology. *Science* **342**, 1094–1098.
- O'Bryan, J.P. (2010). Intersecting pathways in cell biology. *Sci. Signal.* **3**, re10.
- Oeck, S., Malewicz, N.M., Hurst, S., Al-Refae, K., Krysztofiak, A., and Jendrossek, V. (2017). The Focinator v2-0 - Graphical Interface, Four Channels, Colocalization Analysis and Cell Phase Identification. *Radiat. Res.* **188**, 114–120.
- Olivieri, A., and Manzione, L. (2007). Dasatinib: a new step in molecular target therapy. *Ann. Oncol.* **18**, vi42–vi46.
- Olsen, J.V., de Godoy, L.M., Li, G., Macek, B., Mortensen, P., Pesch, R., Markarov, A., Lange, O., Horning, S., and Mann, M. (2005). Parts per million mass accuracy on an Orbitrap mass spectrometer via lock mass injection into a C-trap. *Mol. Cell. Proteomics* **4**, 2010–2021.
- Padmanaban, V., Krol, I., Suhail, Y., Szczerba, B.M., Aceto, N., Bader, J.S., and Ewald, A.J. (2019). E-cadherin is required for metastasis in multiple models of breast cancer. *Nature* **573**, 439–444.
- Piskounova, E., Agathocleous, M., Murphy, M.M., Hu, Z., Huddlestun, S.E., Zhao, Z., Leitch, A.M., Johnson, T.M., DeBerardinis, R.J., and Morrison, S.J. (2015). Oxidative stress inhibits distant metastasis by human melanoma cells. *Nature* **527**, 186–191.
- Porter, R.L., Magnus, N.K.C., Thapar, V., Morris, R., Szabolcs, A., Neyaz, A., Kulkarni, A.S., Tai, E., Chougule, A., Hillis, A., et al. (2019). Epithelial to

- mesenchymal plasticity and differential response to therapies in pancreatic ductal adenocarcinoma. *Proc. Natl. Acad. Sci. USA* **116**, 26835–26845.
- Rappsilber, J., Mann, M., and Ishihama, Y. (2007). Protocol for micro-purification, enrichment, pre-fractionation and storage of peptides for proteomics using StageTips. *Nat. Protoc.* **2**, 1896–1906.
- Schirris, T.J., Renkema, G.H., Ritschel, T., Voermans, N.C., Bilos, A., van Engelen, B.G., Brandt, U., Koopman, W.J., Beyrath, J.D., Rodenburg, R.J., et al. (2015). Statin-Induced Myopathy Is Associated with Mitochondrial Complex III Inhibition. *Cell Metab.* **22**, 399–407.
- Schneider, C.A., Rasband, W.S., and Eliceiri, K.W. (2012). NIH Image to ImageJ: 25 years of image analysis. *Nat. Methods* **9**, 671–675.
- Schug, Z.T., Peck, B., Jones, D.T., Zhang, Q., Grosskurth, S., Alam, I.S., Goodwin, L.M., Smethurst, E., Mason, S., Blyth, K., et al. (2015). Acetyl-CoA synthetase 2 promotes acetate utilization and maintains cancer cell growth under metabolic stress. *Cancer Cell* **27**, 57–71.
- Simpson, C.D., Anyiwe, K., and Schimmer, A.D. (2008). Anoikis resistance and tumor metastasis. *Cancer Lett.* **272**, 177–185.
- Sipos, B., Möser, S., Kalthoff, H., Török, V., Löhr, M., and Klöppel, G. (2003). A comprehensive characterization of pancreatic ductal carcinoma cell lines: towards the establishment of an in vitro research platform. *Virchows Arch.* **442**, 444–452.
- Steeg, P.S. (2006). Tumor metastasis: mechanistic insights and clinical challenges. *Nat. Med.* **12**, 895–904.
- Stone, N.J., Robinson, J.G., Lichtenstein, A.H., Bairey Merz, C.N., Blum, C.B., Eckel, R.H., Goldberg, A.C., Gordon, D., Levy, D., Lloyd-Jones, D.M., et al.; American College of Cardiology/American Heart Association Task Force on Practice Guidelines (2014). 2013 ACC/AHA guideline on the treatment of blood cholesterol to reduce atherosclerotic cardiovascular risk in adults: a report of the American College of Cardiology/American Heart Association Task Force on Practice Guidelines. *Circulation* **129**, S1–S45.
- Stritt, M., Stalder, A.K., and Vezzali, E. (2020). Orbit Image Analysis: An open-source whole slide image analysis tool. *PLoS Comput. Biol.* **16**, e1007313.
- Subramanian, A., Tamayo, P., Mootha, V.K., Mukherjee, S., Ebert, B.L., Gillette, M.A., Paulovich, A., Pomeroy, S.L., Golub, T.R., Lander, E.S., and Mesirov, J.P. (2005). Gene set enrichment analysis: a knowledge-based approach for interpreting genome-wide expression profiles. *Proc. Natl. Acad. Sci. USA* **102**, 15545–15550.
- Szklarczyk, D., Gable, A.L., Lyon, D., Junge, A., Wyder, S., Huerta-Cepas, J., Simonovic, M., Doncheva, N.T., Morris, J.H., Bork, P., et al. (2019). STRING v11: protein-protein association networks with increased coverage, supporting functional discovery in genome-wide experimental datasets. *Nucleic Acids Res.* **47**, D607–D613.
- Tamburrino, D., Crippa, S., Partelli, S., Archibugi, L., Arcidiacono, P.G., Falconi, M., and Capurso, G. (2020). Statin use improves survival in patients with pancreatic ductal adenocarcinoma: A meta-analysis. *Dig. Liver Dis.* **52**, 392–399.
- Tyanova, S., Temu, T., Sinitcyn, P., Carlson, A., Hein, M.Y., Geiger, T., Mann, M., and Cox, J. (2016). The Perseus computational platform for comprehensive analysis of (prote)omics data. *Nat. Methods* **13**, 731–740.
- van Gorsel, M., Elia, I., and Fendt, S.M. (2019). <sup>13</sup>C Tracer Analysis and Metabolomics in 3D Cultured Cancer Cells. *Methods Mol. Biol.* **1862**, 53–66.
- Vizcaíno, J.A., Csordas, A., del-Toro, N., Dianes, J.A., Griss, J., Lavidas, I., Mayer, G., Perez-Riverol, Y., Reisinger, F., Ternent, T., et al. (2016). 2016 update of the PRIDE database and its related tools. *Nucleic Acids Res.* **44**, D447–D456.
- Walker, E.J., Ko, A.H., Holly, E.A., and Bracci, P.M. (2015). Statin use and risk of pancreatic cancer: results from a large, clinic-based case-control study. *Cancer* **121**, 1287–1294.
- Wessel, D., and Flügge, U.I. (1984). A method for the quantitative recovery of protein in dilute solution in the presence of detergents and lipids. *Anal. Biochem.* **138**, 141–143.
- Wickstead, B., and Gull, K. (2011). The evolution of the cytoskeleton. *J. Cell Biol.* **194**, 513–525.
- Wilcox, C.B., Feddes, G.O., Willett-Brozick, J.E., Hsu, L.C., DeLoia, J.A., and Baysal, B.E. (2007). Coordinate up-regulation of TMEM97 and cholesterol biosynthesis genes in normal ovarian surface epithelial cells treated with progesterone: implications for pathogenesis of ovarian cancer. *BMC Cancer* **7**, 223.
- Williams, E.D., Gao, D., Redfern, A., and Thompson, E.W. (2019). Controversies around epithelial-mesenchymal plasticity in cancer metastasis. *Nat. Rev. Cancer* **19**, 716–732.
- Wong, W.W., Tan, M.M., Xia, Z., Dimitroulakos, J., Minden, M.D., and Penn, L.Z. (2001). Cerivastatin triggers tumor-specific apoptosis with higher efficacy than lovastatin. *Clin. Cancer Res.* **7**, 2067–2075.
- Xie, F., Liu, J., Li, C., and Zhao, Y. (2016). Simvastatin blocks TGF- $\beta$ 1-induced epithelial-mesenchymal transition in human prostate cancer cells. *Oncol. Lett.* **11**, 3377–3383.
- Yang, Z., Su, Z., DeWitt, J.P., Xie, L., Chen, Y., Li, X., Han, L., Li, D., Xia, J., Zhang, Y., et al. (2017). Fluvastatin Prevents Lung Adenocarcinoma Bone Metastasis by Triggering Autophagy. *EBioMedicine* **19**, 49–59.
- Yu, R., Longo, J., van Leeuwen, J.E., Mullen, P.J., Ba-Alawi, W., Haibe-Kains, B., and Penn, L.Z. (2018). Statin-Induced Cancer Cell Death Can Be Mechanistically Uncoupled from Prenylation of RAS Family Proteins. *Cancer Res.* **78**, 1347–1357.
- Yuan, S., Norgard, R.J., and Stanger, B.Z. (2019). Cellular Plasticity in Cancer. *Cancer Discov.* **9**, 837–851.
- Zhang, K., Myllymäki, S.M., Gao, P., Devarajan, R., Kytölä, V., Nykter, M., Wei, G.H., and Manninen, A. (2017). Oncogenic K-Ras upregulates ITGA6 expression via FOSL1 to induce anoikis resistance and synergizes with  $\alpha$ V-Class integrins to promote EMT. *Oncogene* **36**, 5681–5694.
- Zhang, J., Li, Q., Wu, Y., Wang, D., Xu, L., Zhang, Y., Wang, S., Wang, T., Liu, F., Zaky, M.Y., et al. (2019a). Cholesterol content in cell membrane maintains surface levels of ErbB2 and confers a therapeutic vulnerability in ErbB2-positive breast cancer. *Cell Commun. Signal.* **17**, 15.
- Zhang, Y., Liang, M., Sun, C., Qu, G., Shi, T., Min, M., Wu, Y., and Sun, Y. (2019b). Statin Use and Risk of Pancreatic Cancer: An Updated Meta-analysis of 26 Studies. *Pancreas* **48**, 142–150.
- Zhao, H., Ross, F.P., and Teitelbaum, S.L. (2005). Unoccupied  $\alpha$ (v) $\beta$ 3 integrin regulates osteoclast apoptosis by transmitting a positive death signal. *Mol. Endocrinol.* **19**, 771–780.

## STAR★METHODS

### KEY RESOURCES TABLE

REAGENT or RESOURCE	SOURCE	IDENTIFIER
<b>Antibodies</b>		
Rabbit monoclonal anti phospho-p44/42 MAPK (Erk1/2) (Thr202/Tyr204) antibody	Cell Signaling Technology	Cat# 4370; RRID:AB_2315112
Rabbit monoclonal anti p44/42 MAPK (Erk1/2) (137F5) Rabbit mAb antibody	Cell Signaling Technology	Cat# 4695; RRID:AB_390779
Rabbit monoclonal anti E-Cadherin (24E10)	Cell Signaling Technology	Cat# 3195; RRID:AB_2291471
Rabbit monoclonal anti GAPDH	Cell Signaling Technology	Cat# 2118; RRID:AB_561053
Rabbit monoclonal anti phospho-smad2 (Ser465/467)	Cell Signaling Technology	Cat# 3108; RRID:AB_490941
Rabbit monoclonal anti phospho-Smad2 (Ser465/467)/Smad3 (Ser423/425) (D27F4)	Cell Signaling Technology	Cat# 8828; RRID:AB_2631089
Rabbit monoclonal anti Smad2 (D43B4)	Cell Signaling Technology	Cat# 5339; RRID:AB_10626777
Rabbit monoclonal anti Smad2/3 (D7G7)	Cell Signaling Technology	Cat# 8685; RRID:AB_10889933
Rabbit monoclonal anti phospho-Src Family (Tyr416)	Cell Signaling Technology	Cat# 2101; RRID:AB_331697
Rabbit monoclonal anti phospho-Src Family (Tyr416) (D49G4)	Cell Signaling Technology	Cat# 6943; RRID:AB_10013641
Rabbit monoclonal anti Src (36D10)	Cell Signaling Technology	Cat# 2109; RRID:AB_2106059
Rabbit polyclonal anti NSDHL	Proteintech	Cat# 15111-1-AP; RRID:AB_2155681
Mouse monoclonal anti Integrin alpha 2	Santa Cruz Biotechnology	Cat# sc-74466; RRID:AB_1124939
Rabbit monoclonal anti Vimentin (D21H3)	Cell Signaling Technology	Cat# 5741; RRID:AB_10695459
Monoclonal mouse anti BrdU (bromodeoxyuridine)	BD Biosciences	Cat# 555627; RRID:AB_10015222
<b>Chemicals, peptides, and recombinant proteins</b>		
Fluvastatin	Abcam	ab120651
Dasatinib	Sigma-Aldrich	SML2589
Tipifarnib	Sigma-Aldrich	SML1668
DMSO	AlliChem	A3672
Mevalonic acid	Sigma-Aldrich	50838
Trametinib	Biomol	GSK-1120212
Cerivastatin	Abcam	ab142853
Lovastatin	Abcam	ab120614
Human TGF-beta 1 Recombinant Protein	Thermo Fisher Scientific	PHG9211
Zoledronic acid	Sigma-Aldrich	SML0223
<b>Deposited data</b>		
Mass spectrometry proteomics data	This paper	PRIDE: <a href="https://www.ebi.ac.uk/pride/archive/">https://www.ebi.ac.uk/pride/archive/</a> Identifier: PXD022345
Microarray data	This paper	NCBI GEO Accession number: GSE161536
Western Blot images	This paper	Mendeley Data: <a href="https://doi.org/10.17632/nn38268p22.1">https://doi.org/10.17632/nn38268p22.1</a>
<b>Experimental models: Cell lines</b>		
Human ASPC1 cells	ATCC	CRL-1682
Human Panc89 cells	RCB	RCB1021
Human PA-TU-8988T cells	DSMZ	ACC-162
Human PA-TU-8988S cells	DSMZ	ACC-204
Human YAPC cells	DSMZ	ACC-382
Human NCL-H1975 cells	ATCC	CRL-5908

(Continued on next page)

<b>Continued</b>		
REAGENT or RESOURCE	SOURCE	IDENTIFIER
Human HCT116 cells	ATCC	CCL-247
Human HEK293T cells	DSMZ	ACC-305
Mouse 0688M cells	liver metastasis of the autochthonous <i>Kras</i> <sup>LSL-G12D/+</sup> ; <i>Trp53</i> <sup>LSL-R172H/+</sup> ; <i>Rosa26</i> <sup>LSL-tdTomato/+</sup> ; <i>Pdx1-Cre</i>	Grüner et al., 2016
Human patient-derived CDX59 cells	This paper	N/A
<b>Experimental models: Organisms/strains</b>		
Immunocompetent 129/B16 F1 mice	The Jackson Laboratory via Charles River	Cross of #002448 and #000664
Immunodeficient NOD/Scid/C (NSG) mice	The Jackson Laboratory via Charles River	#005557
<b>Oligonucleotides</b>		
qPCR Primers, see STAR Methods section	Eurofins	N/A
<b>Recombinant DNA</b>		
shRNA against <i>NSDHL</i> , shNSDHL#1	MISSION® shRNA plasmids, Merck	TRCN0000335871
shRNA against <i>NSDHL</i> , shNSDHL#2	MISSION® shRNA plasmids, Merck	TRCN0000335951
shRNA against <i>NSDHL</i> , shNSDHL#3	MISSION® shRNA plasmids, Merck	TRCN0000335870
MSCV-GFP; PGK Puro	Addgene	#68486
MSCV-6NBC-GFP; PGK Puro	Addgene	#83678 - #83764
VSV-G retro	Addgene	#8454
gag/pol retro	Addgene	#14887
pSPAX2	Addgene	#12260
pMD2.G	Addgene	#12259
<b>Software and algorithms</b>		
Orbit	Stritt et al., 2020	<a href="https://www.orbit.bio/">https://www.orbit.bio/</a>
ImageJ	Schneider et al., 2012	<a href="https://imagej.nih.gov/ij/">https://imagej.nih.gov/ij/</a>
GraphpadPrism	N/A	<a href="https://www.graphpad.com/company/">https://www.graphpad.com/company/</a> Version 7
STRING	Szklarczyk et al., 2019	<a href="https://string-db.org/">https://string-db.org/</a> Version 11.0

## RESOURCE AVAILABILITY

### Lead contact

Further information and requests for resources and reagents should be directed to and will be fulfilled by the lead contact, Barbara M. Grüner ([barbara.gruener@uk-essen.de](mailto:barbara.gruener@uk-essen.de)).

### Materials availability

There are restrictions to the availability of the newly generated human patient-derived cell line CDX59 due to required ethical approval for use in other studies besides the here approved by the ethics committee of the University Duisburg-Essen Medical Faculty.

### Data and code availability

- The mass spectrometry proteomics data for the on-bead digestions has been deposited to the ProteomeXchange Consortium via the PRIDE (Proteomics Identifications (PRIDE), RRID:SCR\_003411) (Vizcaino et al., 2016) partner repository (<https://www.ebi.ac.uk/pride/archive/>) and are publicly available as of the date of publication. Accession numbers are listed in the [Key resources table](#). The microarray data has been deposited at the NCBI GEO (Gene Expression Omnibus) repository and are publicly available as of the date of publication. Accession numbers are listed in the [Key resources table](#). Original western blot images have been deposited at Mendeley and are publicly available as of the date of publication. The DOI is listed in the key resources table. Microscopy data reported in this paper will be shared by the lead contact upon request.
- This paper does not report original code.
- Any additional information required to reanalyze the data reported in this paper is available from the lead contact upon request.

## EXPERIMENTAL MODEL AND SUBJECT DETAILS

### *In vivo* animal studies

All animal experiments were performed in accordance with and approved by the Stanford University Animal Care and Use Committee (for experiments performed at Stanford University) or the Landesamt für Natur, Umwelt und Verbraucherschutz Nordrhein-Westfalen (LANUV) (for experiments performed at University Hospital Essen).

Immunocompetent 129/B16 F1 mice are the offspring of a cross between C57BL/6J (B6, Stock Number #000664 from The Jackson Laboratory via Charles River) and 129S1/SvImJ (129S, Stock Number #002448 from The Jackson Laboratory via Charles River) mice. Immunodeficient NOD/Scid/C (NSG) mice were originally obtained from The Jackson Laboratory via Charles River (Stock Number #005557). Animals were kept in stable groups of 2-5 animals in individually ventilated cages with standard bedding. Water and standard laboratory mouse diet were provided *ad libitum*. Water was filtered into autoclaved bottles. Bedding was regularly changed under a hood to preserve sterile conditions. Light/dark-rhythm was set at 12:12 hours, and room temperature and humidity were kept stable.

For all animal experiments, both male and female adult mice from the age of 8 weeks or older were equally divided and randomly assigned between all experimental groups. All animal experiments and data analyses were performed without blinding and no power analysis was conducted to pre-determine group size. All animals were tagged with ear marks for identification prior to the experiments. No further procedures were performed besides the described experiments in this manuscript.

### Cell lines and primary cultures

All cells were cultured under humidified atmosphere at 37°C and 5% CO<sub>2</sub>. All cell culture experiments were performed in three independent experiments if not mentioned elsewhere. Human ASPC1 cells (ATCC Cat# CRL-1682, RRID:CVCL\_0152, gender: female), Panc89 cells (RCB Cat# RCB1021, RRID:CVCL\_4056, gender: male), also referenced as T3M-4 (Sipos et al., 2003), PA-TU-8988T cells (DSMZ Cat# ACC-162, RRID:CVCL\_1847, female), PA-TU-8988S cells (DSMZ Cat# ACC-204, RRID:CVCL\_1846, gender: female) and YAPC cells (DSMZ Cat# ACC-382, RRID:CVCL\_1794, male) were cultured in DMEM supplemented with 10% FBS, 1% non-essential amino acids, 50 U/ml penicillin and 50 µg/ml streptomycin. Human NCL-H1975 (ATCC Cat# CRL-5908, RRID:CVCL\_1511, female) and PDX (patient derived xenograft) cell line 59 (CDX59, gender: female) were cultured in RPMI supplemented with 10% FBS and 50 U/ml penicillin and 50 µg/ml streptomycin. Human HCT116 (ATCC Cat# CCL-247, RRID:CVCL\_0291, gender: male), HEK293T cells (DSMZ Cat# ACC-305, RRID:CVCL\_0045, gender: female) and mouse cell line 0688M (gender: male, isolated from a liver metastasis of the autochthonous *Kras*<sup>LSL-G12D/+;Trp53</sup><sup>LSL-R172H/+;Rosa</sup><sup>LSL-tdTomato/+;Pdx1-Cre</sup>, described in Grüner et al., 2016) were cultured in DMEM supplemented with 10% FBS and 50 U/ml penicillin and 50 µg/ml streptomycin. All human cell lines have been authenticated by STR analysis. All cell lines were regularly tested to be mycoplasma negative. For compound treatment experiments, cells were seeded for 24 hours and incubated at 37°C and 5% CO<sub>2</sub> to reach a density of 80% at the endpoint of the experiment if not mentioned elsewhere. Cells were then treated with the respective compound or control for the desired time period and incubated at 37°C and 5% CO<sub>2</sub>.

## METHOD DETAILS

### Generation of PDX derived cell line (CDX 59)

After explantation, tumor tissue was stored in RPMI (Life Technologies) without any supplements on ice. The tumor tissue was then minced on ice into 1-2 mm<sup>3</sup> cubes. The minced tissue was then transferred into digestion media (RPMI containing 5 mg/mL Collagenase II (Life Technologies) and 1.25 mg/mL dispase (Life Technologies)) and incubated at 37°C with agitation to dissociate the tumor tissue. Cell suspension was subsequently filtered through a 100 µm mesh and cells were collected by centrifugation (300 xg, 5 min) at room temperature. The cell pellet was resuspended in growth media consisting of 50% Keratinocyte-SFM (Life Technologies) supplemented with Epidermal Growth Factor and Bovine Pituitary Extract (Life Technologies), 2% FBS (Life Technologies), and 1% antibiotic-antimycotic (Life Technologies) and 50% advanced DMEM F12 (Life Technologies) supplemented with 10% FBS (Life Technologies), 10 mM HEPES (Life Technologies), 1% Glutamax (Life Technologies), 1% antibiotic-antimycotic (Life Technologies). Cells were cultured on collagen-coated dishes (Corning) in a humidified incubator at 37°C with 5% CO<sub>2</sub>. To obtain pure PDAC cell lines, cells were treated with differential trypsinization until no contaminating cells were detected by visual inspection under the microscope.

### Chemicals

Compounds used for *in vitro* experiments were commercially available and listed below. Fluvastatin (abcam, ab120651), cerivastatin (abcam, ab142853), trametinib (biomol, GSK-1120212), mevalonic acid (sigma-aldrich, 50838), lovastatin (abcam, ab120614), dasatinib (Sigma-Aldrich, SML2589), tipifarnib (Sigma-Aldrich, SML1668) were solved in DMSO (AppliChem, A3672). The final concentration of DMSO in medium was maximal 1% and DMSO only was used as vehicle control at the same final concentration. Zoledronic acid (Sigma-Aldrich, SML0223) was solved in water (Braun).

### Viral transduction of cells

To generate ASPC1, YAPC, CDX59 and Panc89 cells labeled with GFP we used MSCV retroviral vectors generated using gag/pol-retro and VSV-G-retro packaging plasmids. For shRNA knockdown of *NSDHL* (shNSDHL#1: TRCN0000335871, shNSDHL#2:

TRCN0000335951, shNSDHL#3: TRCN0000335870) and control in ASPC1, YAPC and Panc89 we used MISSION® shRNA plasmids (Merck) plus pSPAX2 and pMD2.G packaging plasmids. For virus production, HEK293T cells were seeded into 6-well plates and individual wells were transfected at 80% confluency with plasmid vector and packaging plasmids using TransIT®-TKO or TransIT®-LT1 Transfection Reagent (Mirus). Media was changed 24 hours later. Supernatants were collected at 48 and 72 hours, pooled, centrifuged for 10 minutes at 13,200 rpm and the undiluted supernatants were each applied to a 70% confluent well cells. Two days after infection the cells were selected with puromycin (1–3  $\mu\text{g}/\text{mL}$ ), which effectively kills all uninfected cells. After puromycin selection, GFP expression was tested using flow cytometry.

### Immunofluorescence (Actin and E-cadherin staining)

For imaging of fixed cells, cells were plated onto collagen type-I-coated glass-bottom dishes (1 h,  $c = 0.01 \text{ mg}/\text{ml}$ ). The cells were treated in triplicate with fluvastatin or vehicle control for 48 h.

To stain for actin cytoskeleton, cells were fixed by adding formaldehyde-PBS directly to the media to a final concentration 4%, and incubated for 20 min at 37°C. Coverslips were washed three times with PBS and permeabilized with 0.1% Triton X-100 for 10 min at room temperature. Coverslips were incubated with Phalloidin-Tetramethylrhodamine B (1:500; 35545A, Sigma-Aldrich) for 45 min at room temperature followed by three times washing with PBS.

To stain for E-cadherin, cells were fixed with ice-cold methanol. To remove methanol coverslips were washed three times with PBS. Unspecific binding of antibody was blocked by incubating coverslips with 2%-BSA-PBS for 1 h. E-cadherin primary antibody (BD Biosciences Cat# 610181, RRID:AB\_397580, 1:500) was incubated for 1 h at room temperature. Coverslips were washed three times with PBS before incubating with secondary antibody (goat-anti-mouse-Alexa488; Molecular Probes Cat# A-11029, RRID:AB\_138404, 1:500 in 2% BSA-PBS) at room temperature. Coverslips were incubated for 10 min at RT with 4',6-Diamidino-2'-phenylindole dihydrochloride (DAPI, 1:1000, AppliChem) to stain nuclei. To quench unbound aldehydes coverslips were post-fixed with 2% formaldehyde-PBS. Samples were washed with distilled water and mounted on glass slides using ProLong Gold antifade reagent (Invitrogen).

Confocal laser scanning microscopy of fixed cells was performed on a TCS SP8 AOBS system (Leica Microsystems) equipped with an HC PL APO 20  $\times$  /0.75 NA CS objective. Excitation of rhodamine-phalloidin was performed using a 561-nm line laser. Fluorescence was measured using HyD detector (570–630 nm). Excitation of E-cadherin was performed using a 488-nm line of an argon laser. Fluorescence was measured using the HyD detector (495–540 nm). Excitation for DAPI was performed using a 405-nm line with the diode laser and fluorescence was measured using PMT detector (415–440 nm). Acquisition was controlled using LASAF software with HCS-A Matrix Screener module for automated imaging (Leica Microsystems). Confocal z stacks were acquired with 210-nm spacing. Stack building and maximum and sum projections were generated with ImageJ software (ImageJ, RRID:SCR\_003070).

### Live cell imaging and live cell tracking

For live cell imaging, cells were plated on  $\mu$ -Slide VI 0.4 (Ibidi). Microscope used for live-cell imaging is equipped with temperature-controlled incubation chamber and time-lapse live-cell microscopy experiments were performed at 37°C in CO<sub>2</sub>-independent medium (HBSS buffer, 10% FBS, 1% non-essential amino acids, 2 mM l-Glutamine, 10 mM HEPES, 1 mM MgCl<sub>2</sub>, and 1 mM CaCl<sub>2</sub>) with indicated frame rates. Phase contrast microscopy was performed using an inverted Ti eclipse system (Nikon). Images were acquired using a Roper Scientific CoolSNAP HQ2 interline-transfer CCD camera. Phase-contrast images were acquired using a CFI S Plan Fluor ELWD 20x/0.45 DIC objective (Nikon). NIS Elements software (Nikon) controlled image acquisition.

Cell migration of ASPC1 and Panc89 cells treated for 48 h with vehicle or fluvastatin (5  $\mu\text{M}$ ) was analyzed. Phase contrast imaging was performed for 180 min (framerate 1/min). Image Stabilizer PlugIN (ImageJ (ImageJ, RRID:SCR\_003070)) was used for stage moving correction. Quantification of cells was performed by using manual tracking PlugIN (ImageJ). Tracking of cell nuclei was performed only if cells showed more than 50% free leading edge, no multi-nuclei, no overlapping, and were not dividing during imaging. The chemotaxis and migration tool (Ibidi) was used to show cell migration (accumulated distance and velocity). ASPC1 cells:  $n = 59$ –65 cells and Panc89 cells:  $n = 57$ –61 cells from three individual experiments. \*\*\*,  $p < 0.001$ ; unpaired t test.

### <sup>13</sup>C-labeling experiments

#### *In vitro* treatment

ASPC1 cells were seeded in triplicate in 6 well plates. The next day cells were treated for 48 h with 5  $\mu\text{M}$  fluvastatin (Abcam) or the respective control in medium supplemented with 4.5g/L <sup>13</sup>C-Glucose (Sigma-Aldrich). After treatment medium was removed, cells were washed twice with 0.9% NaCl buffer, snap-frozen with liquid nitrogen and stored at –80°C.

#### Metabolites extraction and derivatization method

Metabolite extraction were performed in a mixture ice - dry ice as described before (van Gorsel et al., 2019; Elia et al., 2017).

Briefly, cells were extracted with 800  $\mu\text{L}$  of methanol/water (5:3) (v/v) and a volume of 500  $\mu\text{L}$  of precooled chloroform containing 10  $\mu\text{g}/\text{ml}$  of C17 internal standard was added to each sample. Therefore, samples were vortexed for 10 min at 4°C and centrifuged for other 10 min (max. speed, 4°C). After centrifugation, metabolites were separated in two phases divided by a protein layer: polar metabolites in the methanol/water (upper) phase and the lipid fraction in the chloroform (lower) phase. The lipid fraction was further separated in two reactions with equal volumes for the analysis of cholesterol and fatty acids. Afterward, every phase was dried at 4°C overnight using a vacuum concentration.

The samples were derivatized and measured as described before (Lorendeau et al., 2017). Fatty acid samples were esterified with 500  $\mu$ L 2% sulfuric acid in methanol overnight at 50°C. Fatty acids were then extracted by addition of 600  $\mu$ L of hexane and 100  $\mu$ L of saturated NaCl. Samples were centrifuged for 5 min, the hexane phase was separated and dried with a vacuum concentrator. Fatty acid samples were then resuspended in 50  $\mu$ L of hexane. Cholesterol samples were saponified with 500  $\mu$ L 20% w/v of sodium hydroxide in 50% ethanol at 97°C for 5 min, and the unsaponifiable fraction containing cholesterol was extracted with 600  $\mu$ L hexane and dried in a vacuum concentrator. The samples were then resuspended in 20  $\mu$ L of pyridine and 7.5  $\mu$ L of samples were transferred into a vial and derivatized with 15  $\mu$ L of trimethylsilyl (TMS) for 1 hour at 40°C.

### Gas chromatography–mass spectrometric analysis

The metabolites were analyzed by gas chromatography (8860 GC system) coupled to mass spectrometry (5977B Inert MS system) from Agilent Technologies. The inlet temperature was set at 270°C and 1  $\mu$ L of samples were injected in splitless mode. Metabolites were separated with a DB-FASTFAME column (30 m x 0.250 mm). Helium was used as a carrier gas with a flow rate of 1 mL/min. For the separation of fatty acids, the initial gradient temperature was set at 50°C for 1 min and increased at the ramping rate of 12°C/min to 180°C, following by a ramping rate of 1°C/min to reach 200°C. Finally, the final gradient temperature was set at 230°C with a ramping rate of 5°C/min for 2 min. For the measurement of cholesterol, the oven was set at 100°C for 1 min, ramped to 220°C at 20°C/min, following by a ramping of 5°C/min to reach 250°C. The temperatures of the quadrupole and the source were set at 150°C and 230°C, respectively. An electron impact ionization fixed at 70 eV was applied and a full scan mode was used for the measurement of cholesterol and fatty acid, ranging from 200 to 500 a.m.u (mass) and from 100 to 400 a.m.u (mass), respectively.

### Data analysis – MATLAB

After the acquisition by GC-MS, an inhouse MATLAB (MATLAB, RRID:SCR\_001622) M-file was used to extract mass distribution vectors and integrated raw ion chromatograms. The natural isotopes distribution were also corrected using the method developed by Fernandez et al. (1996). The peak area was subsequently normalized to the protein content and to the internal standard: C17. Palmitate synthesis were calculated based on isotopologue distributions of the according fatty acid, using Isotopomer Spectral Analysis (ISA) (Kharroubi et al., 1992) and an in-house MATLAB script (available on request). Overall levels of labeled palmitate were equal in all treatment groups, indicating that the labeling itself had no effect on cholesterol synthesis (Figure S3C).

### Spheroid formation assay

Unless otherwise stated cells were treated in triplicate for 48 h with compound of interest or the respective control. To initiate formation of spheroids cells were seeded in triplicate ( $8 \times 10^3$ – $20 \times 10^3$  cells/well) into commercially available cell culture plates with cell-repellent surface (CELLSTAR®, 650970) in medium with drug or vehicle control treatment. Spheroids were grown for 24 h or up to 7 days and pictures taken using Primovert microscope (Zeiss). Spheroids were quantified using ImageJ (ImageJ, RRID:SCR\_003070) as previously described in Oeck et al. (2017).

### Assessment of *in vitro* viability

Cells were seeded in triplicate per condition into 96-well plates ( $8 \times 10^3$ – $20 \times 10^3$  cells/well). Compounds were added in different concentrations in triplicate wells. After 0, 24, 48 and 72 hours, cell viability was assessed using the PrestoBlue cell viability assay (A13262, Invitrogen) per manufacturer's instructions and absorbance at 570 and 600 nm was assessed using a Tecan Spark 10M plate reader (Tecan Trading AG).

### Annexin V staining

To assess apoptosis, cells were treated in triplicate for 48 h with compound of interest or the respective control in triplicate and stained for Annexin V according to the manufacturer's instructions using FITC Annexin V (BD Biosciences Cat# 556419, RRID:AB\_2665412). Analysis was done on a BD FACSCelesta Analyzer (Becton, Dickinson and Company).

### Anoikis survival assay

To assess anoikis of the cells and to prevent cells from adhering, 6 well plates were coated using a PolyHEMA (Sigma-Aldrich) stock solution (20 mg/ml in 95% EtOH). Cells were pretreated for 48 h with the compound of interest or the respective control, counted and seeded in triplicate with the respective treatment in coated wells and in uncoated wells as apoptosis control. After 24 h of incubation cells were stained for Annexin V (BD Biosciences Cat# 556419, RRID:AB\_2665412) to monitor apoptosis using a BD FACSCelesta Analyzer (Becton, Dickinson and Company) as described above. For analysis, the percentage of apoptotic cells of the coated control wells was normalized to the uncoated wells.

### Cell cycle analysis

For cell cycle analysis, cells were treated in triplicate for 48 h with the compound of interest or the respective control in triplicate. Cells were fixed in 4% Paraformaldehyde for 15 min and permeabilized with 0.5% Triton X-100 for 5 min. To visualize DNA content cells were stained with DAPI (AppliChem) and analyzed using a FACS Fortessa Analyzer (BD Biosciences).

### Colony formation assay

For colony formation assay, cells were treated for 48 h with the compound of interest or the respective control. Cells were seeded in triplicate under drug treatment in triplicate at 2000 cells per well in a 6 well plate. Cells were cultivated at 37°C up to three weeks until colonies were visible. Colonies were washed with PBS and stained for 10–30 minutes with Crystal violet. Colonies were automatically counted using ImageJ software (ImageJ, RRID:SCR\_003070).

### Microarray analysis

For microarray analysis, ASPC1-GFP cells were treated in triplicate for 48 h with 5 μM fluvastatin or the respective control. After treatment cells were harvested and cell pellets were stored at –80°C. RNA isolation was performed using the QIAGEN kit according to the manufacturer's manual and stored at –80°C. Affymetrix chip Clariom S Human analysis and normalization of the samples was performed according to standard protocols (DKFZ Heidelberg Genomics and Proteomics Core Facility). A fold change of ± 1.2, p value < 0.05 was considered significant.

### Gene set enrichment analysis

For gene set enrichment analysis (GSEA, (Gene Set Enrichment Analysis, RRID:SCR\_003199)) the software version GSEA\_4.0.3 was used (Mootha et al., 2003; Subramanian et al., 2005). All analyzed gene sets and the software were downloaded from the official GSEA website (the Broad). To perform the analyses, normalized microarray data of ASPC1-GFP cells treated with 5 μM fluvastatin (Abcam) or the respective control was used. An FDR of 0.25 and a p value < 0.05 was considered significant.

### Proteome and phosphorylated proteome analysis

#### *In vitro treatment*

For total proteome analysis, ASPC1-GFP cells were treated in quadruplicate for 48 h with 5 μM fluvastatin (Abcam) or the respective control. To analyze the phosphorylated proteome ASPC1-GFP cells were treated in quintuplicate for 48 h with 5 μM fluvastatin (Abcam) or the respective control and for 15 min with 5 μM fluvastatin (Abcam) or the respective control. After treatment, cells were harvested and cell pellets were stored at –80°C.

#### *Sample preparation for LC/MS/MS*

Frozen cell pellets treated with fluvastatin or DMSO (control) were ground in 1 × PBS and then sonicated using a Bioruptor (Diagenode, 4°C, 10 cycles each 1 min maximum energy followed by 30 s pause). The samples were then cleared by centrifugation (20800 × g, 60 min, 4°C) and the supernatant transferred to a fresh Eppendorf tube. Protein concentration was determined using a modified Bradford assay (Roti-Nanoquant®). A volume corresponding to 30 μg of protein was removed for each sample and Methanol/Chloroform precipitated (Wessel and Flügge, 1984). The protein pellet was rehydrated in 6 M Urea and the proteins were subjected to in-solution digestion (ISD). Briefly, proteins were reduced with DTT (5 mM) in 6 M urea and 50 mM ammonium bicarbonate (ABC) for 30 min at room temperature. Protein reduction was followed by alkylation with iodoacetamide (IAM, 10 mM in 50 mM ABC, 30 min, room temperature) and quenching of excess IAM with DTT (final concentration DTT 10 mM). Samples were digested with LysC for 3 h at 37°C. After adjusting the urea concentration to 0.8 M urea with 50 mM ABC the samples were digested for 16 h with trypsin at 37°C. The digestion was stopped by adding formic acid (FA) to a final concentration of 0.5%. The supernatant, containing the digestion products, was passed through home-made glass microfiber StageTips (GE Healthcare, RRID:SCR\_000004; poresize: 1.2 μm; thickness: 0.26 mm). Cleared tryptic digests were then desalted on home-made C18 StageTips as described (Rapsilber et al., 2007). Briefly, peptides were immobilized and washed on a two disc StageTip. After elution from the StageTips, samples were dried using a vacuum concentrator (Eppendorf) and the peptides were taken up in 0.1% formic acid solution (10 μL) and directly used for LC-MS/MS experiments (see below for details).

#### *Phosphopeptide enrichment*

Phosphopeptides were enriched as described (Humphrey et al., 2015) with slight modifications. Briefly, frozen cell pellets treated with fluvastatin or DMSO (control) were ground in 1 mL GdmCl lysis buffer (6 M guanidine hydrochloride (GdmCl), 100 mM, Tris pH 8.5, 10 mM TCEP, 40 mM CAA) and boiled for 15 min at 95°C. Since GdmCl lysis buffer already contains TCEP and CAA, no further reduction or alkylation of proteins was necessary. Subsequently, the lysate was sonicated (Bioruptor, Diagenode, high voltage, 30 s pulse, 30 s pause, 4°C) and boiled again as described above. To remove remaining cell debris, the lysate was cleared by centrifugation (20800 × g, 30 min, 4°C) and the supernatant transferred to a fresh reaction tube. Proteins were precipitated using MeOH-chloroform precipitation (Wessel and Flügge, 1984). The resulting protein pellet was solubilized in 500 μL 10% 2,2,2-trifluoroethanol (TFE, in 100 mM ammonium bicarbonate). To support solubilization, the protein pellet was ground and sonicated as described above. Protein concentration was determined using a modified Bradford assay (Roti-Nanoquant®) as described in the manufacturer's protocol. An equivalent of 800 μg protein was transferred to a fresh tube and digested with a 1:1 mix of Lys-C and trypsin (ratio 1:50 enzyme to protein, 16 h, 37°C). Undigested proteins were removed by centrifugation (18000 × g, 30 min, 4°C). Phosphopeptide enrichment was performed using the cleared digest. To this end, TiO<sub>2</sub> coupled Sepharose beads (ratio 1:10 protein to beads, GL Sciences #5020-75010) were added. Beads and phosphopeptides were incubated for 15 min at 40°C. After centrifugation, the supernatant (containing non-phosphopeptides) was discarded. To remove unspecifically bound peptides, beads were washed five times with washing buffer (60% ACN/1% TFA). The bead pellet was suspended in 80% ACN/0.05% acetic acid and loaded onto a C8 StageTip and centrifuged until no liquid remained (5 min at 300 × g). Finally, phosphopeptides were eluted using a 40% ACN and 3% NH<sub>4</sub>OH elution buffer. The

eluate was concentrated to about 20  $\mu$ L and desalted using styrenedivinylbenzene–reversed phase sulfonated (SDB-RPS, 3M Empore) StageTips (Rappsilber et al., 2007). For this, the acidified (0.2% TFA) phosphopeptides were immobilized on SDB-RPS Stage-Tips by centrifugation (5 min at 500  $\times$  g), then washed two times with 0.2% TFA and finally eluted using the 40% ACN and 3%  $\text{NH}_4\text{OH}$  elution buffer. The resulting eluate was dried using a vacuum concentrator (Eppendorf) and stored until further use at  $-20^\circ\text{C}$ . Immediately before MS analysis the phosphopeptide samples were solubilized in 10  $\mu$ L 0.1% formic acid.

#### LC-MS/MS settings

Experiments were performed on an Orbitrap LUMOS instrument (Thermo Fisher Scientific) coupled to an EASY-nLC 1200 ultra-performance liquid chromatography (UPLC) system (Thermo Fisher Scientific). The UPLC was operated in the one-column mode. The analytical column was a fused silica capillary (75  $\mu\text{m} \times 46\text{ cm}$ ) with an integrated PicoFrit emitter (New Objective) packed in-house with Reprosil-Pur 120 C18-AQ 1.9  $\mu\text{m}$  resin (Dr. Maisch). The analytical column was encased by a column oven (Sonation PRSO-V2) and attached to a nanospray flex ion source (Thermo Fisher Scientific). The column oven temperature was set to  $50^\circ\text{C}$  during sample loading and data acquisition. The LC was equipped with two mobile phases: solvent A (0.1% formic acid, FA, in water) and solvent B (0.1% FA in 80% acetonitrile, ACN). All solvents were of UPLC grade (Sigma-Aldrich). Peptides were directly loaded onto the analytical column with a maximum flow rate that would not exceed the set pressure limit of 980 bar (usually around 0.5–0.8  $\mu\text{L}/\text{min}$ ). Peptides from full proteome samples were subsequently separated on the analytical column by running a 105 min gradient of solvent A and solvent B (start with 9% B; gradient 9% to 40% B for 90 min; gradient 40% to 100% B for 10 min and 100% B for 5 min). Phosphoproteome samples were separated on the analytical column by running a 140 min gradient of solvent A and solvent B (start with 5% B; gradient 5% to 40% B for 120 min; gradient 40% to 100% B for 10 min and 100% B for 5 min). The flow rate for both gradients was 300 nL/min.

The mass spectrometer was controlled by the Orbitrap Fusion Lumos Tune Application (version 3.3.2782.28) and operated using the Xcalibur (Thermo Xcalibur, RRID:SCR\_014593 software) (version 4.3.73.11). The mass spectrometer was set in the positive ion mode. Precursor ion scanning was performed in the Orbitrap analyzer (FTMS; Fourier Transform Mass Spectrometry) in the scan range of  $m/z$  375–1500 and at a resolution of 120000 with the internal lock mass option turned on (lock mass was 445.120025  $m/z$ , polysiloxane) (Olsen et al., 2005). For full proteome analysis product ion spectra were recorded in a data dependent fashion in the ion trap (ITMS) in a variable scan range and at turbo scan rate. For phosphoproteome samples product ion spectra were recorded in a data dependent fashion in the Orbitrap (OTMS) in a variable scan range and at resolution 30000.

The ionization potential (spray voltage) was set to 2.3 kV. Peptides were analyzed using a “Top Speed” regime (repeating cycle of full precursor ion scan (AGC target “standard” or 50 ms) followed by dependent MS2 scans for 3 s (minimum intensity threshold  $3 \times 10^3$ ). The precursor ions were isolated using the quadrupole (isolation window 1.2  $m/z$ ). After Higher-energy C-trap dissociation (HCD) (normalized collision energy set to “fixed” and 30%) the product ions were measured in the ion trap (full proteome samples, normalized AGC target 300% or 60 ms, mass range “auto”) or in the Orbitrap (phosphoproteome samples, normalized AGC target “standard” or 54 ms, mass range “auto”). During MS2 data acquisition dynamic ion exclusion was set to 120 s. Only charge states between 2–7 were considered for fragmentation.

#### Peptide and Protein Identification using MaxQuant

RAW spectra were submitted to an Andromeda (Cox et al., 2011) search in MaxQuant (1.6.10.43) (MaxQuant, RRID:SCR\_014485) using the default settings (Cox and Mann, 2008). Label-free quantification and match-between-runs was activated (Cox et al., 2014). For *H. sapiens* we used the uniprot reference database (UP000005640\_9606.fasta, 20668 entries, one protein sequence per gene, downloaded from 10/24/2019). All searches included a contaminants database search (as implemented in MaxQuant, 245 entries). The contaminants database contains known MS contaminants and was included to estimate the level of contamination. Andromeda searches allowed oxidation of methionine residues (16 Da), acetylation of the protein N terminus (42 Da) and for phosphoproteomics samples Phospho (STY) as dynamic modifications and the static modification of cysteine (57 Da, alkylation with iodoacetamide). Enzyme specificity was set to “Trypsin/P” with two missed cleavages allowed. The instrument type in Andromeda searches was set to Orbitrap and the precursor mass tolerance was set to  $\pm 20$  ppm (first search) and  $\pm 4.5$  ppm (main search). The MS/MS match tolerance was set to  $\pm 0.5$  Da. The peptide spectrum match FDR and the protein FDR were set to 0.01 (based on target-decoy approach). Minimum peptide length was 7 amino acids. For protein quantification unique and razor peptides were allowed. Modified peptides were allowed for quantification. The minimum score for modified peptides was 40. Label-free protein quantification was switched on, and unique and razor peptides were considered for quantification with a minimum ratio count of 2. Retention times were recalibrated based on the built-in nonlinear time-rescaling algorithm. MS/MS identifications were transferred between LC-MS/MS runs with the “match between runs” option in which the maximal match time window was set to 0.7 min and the alignment time window set to 20 min. The quantification is based on the “value at maximum” of the extracted ion current. At least two quantitation events were required for a quantifiable protein. For full proteome experiments further analysis and filtering of the results was performed in Perseus v1.6.2.3. (Perseus, RRID:SCR\_015753) (Tyanova et al., 2016) For quantification we combined related biological replicates to categorical groups and investigated only those proteins that were found in at least one categorical group in a minimum of 3 out of 4 biological replicates. Comparison of protein group quantities (relative quantification) between different MS runs is based solely on the LFQ’s as calculated by MaxQuant, MaxLFQ algorithm (Cox et al., 2014). A fold change of  $\pm 1.2$ , with  $p$  value  $< 0.05$  was considered significant.

In order to determine phosphorylation sites after treatment, Phospho (STY).txt file was loaded into Perseus v1.6.10.0 (Perseus, RRID:SCR\_015753) (Tyanova et al., 2016). First, only phosphorylation sites with localization probability  $\geq 0.7$  were considered valid

and phosphorylation sites with localization probability less than 0.7 were rejected from the matrix. For quantification, related biological replicates were combined to categorical groups. Subsequently, phosphorylation site abundances were normalized to median intensity per replicate. Only phosphorylation sites that appear in 3 out of 5 related replicates in at least one categorical group were further investigated. To elucidate significant alterations in different categorical groups, a student's test ( $p$  value  $\leq 0.05$ ) was conducted. In order to identify significant alterations of phosphorylation sites missing in one categorical group, missing values were imputed from Gaussian distribution (width = 0.3, down-shift = 1.8). Again, significance was tested with Student's  $t$  test as described above. Only phosphorylation sites with significant changes in the non-imputed and imputed dataset were considered valid. These valid phosphorylation sites were used for STRING (STRING, RRID:SCR\_005223) protein network analysis.

### STRING analysis

For STRING (STRING, RRID:SCR\_005223) analysis, the online software version 11.0 (<https://string-db.org/>) was used. For the significantly up- or downregulated matched genes/proteins of the microarray and proteome analysis were identified and combined with the significantly up- or downregulated proteins of the phosphorylated proteome analysis after 48 h and 15 min. Confidence intervals were set at 0.9.

### EMT-States comparison analysis

Expression values from microarray analysis of both DMSO and fluvastatin-treated samples were averaged over all 3 replicates per treatment group for the identified marker genes. The resulting mean values were log<sub>2</sub>-transformed. In order to compare the resulting values for fluvastatin-treated and DMSO-treated cells with the mean expression values gathered from literature (Karacosta et al., 2019), a comparable value for every marker gene was computed by dividing the expression value of the marker gene by the complete expression of all marker genes in the respective cell state, resulting in a percentage score normalized toward the absolute expression value of every state.

### Western Blot

Unless otherwise stated cells were treated for 48 h with compound of interest or the respective control. After treatment cells were harvested and proteins were isolated using RIPA lysis buffer according to standard protocols. For protein electrophoresis and blotting standard protocols, Precast Gels (Bio-Rad, 4568086, 4561084) and the Trans-Blot Turbo Transfer System (Bio-Rad) were used. Antibodies were purchased from Cell Signaling Technology (phospho Erk (Cell Signaling Technology Cat# 4370, RRID:AB\_2315112, 1:1000), Erk (Cell Signaling Technology Cat# 4695, RRID:AB\_390779, 1:1000), E-cadherin (Cell Signaling Technology Cat# 3195, RRID:AB\_2291471, 1:1000), GAPDH (Cell Signaling Technology Cat# 2118, RRID:AB\_561053, 1:10000), phospho Smad-2 (Cell Signaling Technology Cat# 3108, RRID:AB\_490941, 1:1000), phospho Smad-2/3 (Cell Signaling Technology Cat# 8828, RRID:AB\_2631089, 1:1000), Smad-2 (Cell Signaling Technology Cat# 5339, RRID:AB\_10626777, 1:1000), Smad-2/3 (Cell Signaling Technology Cat# 8685, RRID:AB\_10889933, 1:1000), phospho Src (Cell Signaling Technology Cat# 2101, RRID:AB\_331697, 1:1000), phospho Src (Cell Signaling Cat# 6943, RRID:AB\_10013641; 1:1000), Src (Cell Signaling Technology Cat# 2109, RRID:AB\_2106059, 1:1000)), NSDHL (Proteintech Cat# 15111-1-AP, RRID:AB\_2155681, 1:1000) and from Santa Cruz Biotechnology (Integrin alpha 2 (Santa Cruz Biotechnology Cat# sc-74466, RRID:AB\_1124939, 1:1000)). GAPDH was used for all experiments as a loading control.

### Quantitative real-time PCR (qRT-PCR)

Unless otherwise stated cells were treated for 48 h with compound of interest or the respective control. After treatment cells were harvested and RNA was isolated, purified with Rneasy Mini Kit (QIAGEN) and reversely transcribed as per the manufacturer's protocols.

qRT-PCR was performed using LightCycler® 480 SYBR Green I Master Kit (Roche) according to standard protocols and manufacturer's instructions. Analysis was performed in triplicate and relative expression was calculated with  $\Delta\Delta$ CT method. Actin or GAPDH expression was used for normalization.

Primer sequences:

Actin: fw GGA TTC CTA TGT GGG CG, rv GGC GTA CAG GGA TAG  
 CDH1: fw CAGTTCCGAGGTCTACACCTT, rv TGAATCGGGAGTCTTCCGAAA  
 HMGCR: fw GACAAAGAATTGACAGGCTTG, rv CTGAGGGCAAACCTTTGCTAATG  
 SNAI2: fw TCCAAACCCACTCGGATGTGAAGA, rv TTGGTGCTTGTGGAGCAAGGACAT  
 GAPDH: fw CCACCCATGGCAAATCCATGGCA, rv TCTAGACGGCAGGTCAGGTCCACC  
 NSDHL: fw AGGCAGCCAGGAACGGCAAGAT, rv GAAATGCCTTCCCACCCAGTGTGCA

### In vivo experiments

#### In vivo multiplexed screening for metastatic seeding

In vivo multiplexed screening of the FDA library of approved drugs was performed and analyzed as described in Grüner et al. (2016) in barcoded variants of the murine 0688M cell line, the human Panc89 or ASPC-1 cell line. In brief, each compound plate contained ~72

compounds and ~24 DMSO containing control wells. 2  $\mu\text{L}$  of each compound were added to the barcoded cells using an Agilent (formerly Velocity11) vertical pipetting station with a 96LT pipetting head to a final concentration of 10  $\mu\text{M}$ . Each compound plate was tested on one barcoded cell plate. While short-term treatment with covalent inhibitors leads to long-term target inhibition (Grüner et al., 2016), we reasoned that longer-term treatment with any class of inhibitors could lead to gene expression and signaling changes that could impact metastatic seeding. Therefore, we initially used a pretreatment time of ~40 hours to increase our chance of generating a sustained inhibitory effect, based on transcriptional, translational and signaling changes after pooling. Cells were treated for ~40 hours at 37°C, media was removed, cells were washed once with PBS, and trypsinized for 5 minutes. All cells of one plate were pooled, centrifuged, counted, and diluted to approximately  $5 \times 10^6$  cells per ml in PBS. 100  $\mu\text{L}$  of cells (~ $10^6$ ) from each plate were injected into the lateral tail vein of one 129/B16 F1 or NOD/Scid/C (NSG) mouse. The remaining cells (~200  $\mu\text{L}$ ) were pelleted and frozen for pre-injection barcode representation analysis. The rescreen of the 30 top compounds was performed twice once with 48 h and once with 72 h of drug pretreatment with 10, 5, 2.5 and 1  $\mu\text{M}$  of each compound. Extraction of barcoded cells from the lungs, DNA extraction, PCR amplification of barcodes, library preparation, Next generation sequencing (NGS) analysis and bioinformatics analysis were performed as described previously (Grüner et al., 2016). A reduction of metastatic ability of 20%, which corresponds to ~3 times the standard deviation of DMSO treated cells, was considered significant.

#### **In vivo drug treatment metastasis assay**

For subcutaneous injections  $0.25 \times 10^6$  ASPC1 cells in 100  $\mu\text{L}$  PBS/matrigel 1:1 were injected into each flank of NOD/Scid/C (NSG) mice. Subcutaneous tumors were observed and tumor size was measured at approximately 10 days after injection when tumors had volumes between 50 and 120  $\text{mm}^3$ . Then mice were randomly divided into groups of equal tumor volume and daily treated per oral gavage with 20 mg/kg fluvastatin (Hexal®) or vehicle control once per day. Mice were analyzed after 35 days of treatment. Lung lobes were imaged from both sides using the AxioVert stereomicroscope (Zeiss). Then, two lung lobes were preserved for histological analysis, the other three lung lobes were minced using scissors and digested for 1 hour at 37°C in digestion media with 10% trypsin (0.25% in EDTA, Invitrogen), 10% collagenase IV (10 mg/ml in HBSS, Worthington) and 10% dispase (Corning) in HBSS w/o  $\text{Ca}^{2+}$  and  $\text{Mg}^{2+}$ . Digest was quenched with L15 media (Invitrogen) containing 10% FBS and DNase (5 mg/ml in HBSS) and suspension was filtered through a 40  $\mu\text{m}$  mesh, centrifuged, washed, and filtered again. Samples were analyzed for GFP expression by FACS on a Fortessa analyzer (BD Biosciences). No statistical method was used to predetermine sample size.

#### **In vivo tumor formation and blood stream survival experiment**

To assess *in vivo* tumor formation, cells were pretreated with the compound of interest or the respective control for 48 h. Depending on the cell line used  $0.5 \times 10^6$  to  $2.5 \times 10^6$  cells were injected subcutaneously into each flank or intravenously into the lateral tail vein of NOD/Scid/C (NSG) mice. To control for equal cell numbers between the different pretreated cells, an equal number of cells was mixed with the same volume of counting beads (CountBright, Invitrogen) and analyzed by FACS on a Fortessa analyzer (BD Biosciences). The same batch of cells was always used for both the intravenous and the subcutaneous injection within one experiment. 10 to 14 days after injection mice were sacrificed and analyzed for tumor size and weight (subcutaneous injection) or number of cancer cells in the lungs (intravenous injection). Lungs were processed and analyzed as described above. No statistical method was used to predetermine sample size.

#### **Histology and immunohistochemistry**

Tissue samples were fixed in 4% formalin and paraffin embedded. Hematoxylin and eosin staining was performed using standard methods. Immunohistochemistry was performed using standard methods and standard antigen unmasking (1 mM citrate buffer pH 6). Primary immunoblotting antibodies were against GFP (Abcam Cat# ab6673, RRID:AB\_305643, 1:1000 dilution), Ki67 (Abcam Cat# ab15580, RRID:AB\_443209, 1:1000 dilution), E-cadherin (Cell Signaling Technology Cat# 3195, RRID:AB\_2291471, 1:200), Vimentin (Cell Signaling Technology Cat# 5741, RRID:AB\_10695459, 1:100) and BrdU (BD Biosciences Cat# 555627, RRID:AB\_10015222, 1:500 dilution). Percent tumor area was calculated using Orbit Image analysis and ImageJ software (ImageJ, RRID:SCR\_003070).

#### **QUANTIFICATION AND STATISTICAL ANALYSIS**

Graphs and statistics were generated using the GraphPad Prism software (GraphPad Prism, RRID:SCR\_002798). Significance was calculated as indicated in the figure legends: not indicated = not significant, \*  $p < 0.05$ , \*\*  $p < 0.01$ , \*\*\*  $p < 0.001$ . At least two (*in vivo*) or three (*in vitro*) independent experiments were performed for each analysis. Statistical tests, dispersion and precision measures, and number of samples and/or repeats are indicated in the STAR Methods and figure legends for each assay and analysis.

# DuEPublico

Duisburg-Essen Publications online

UNIVERSITÄT  
DUISBURG  
ESSEN

*Offen im Denken*

ub

universitäts  
bibliothek

This text is made available via DuEPublico, the institutional repository of the University of Duisburg-Essen. This version may eventually differ from another version distributed by a commercial publisher.

**DOI:** 10.1016/j.celrep.2021.110056

**URN:** urn:nbn:de:hbz:465-20220801-103049-8



This work may be used under a Creative Commons Attribution - NonCommercial - NoDerivatives 4.0 License (CC BY-NC-ND 4.0).